Understanding the microstructure and mechanical performance of heat-treated Inconel 625/TiC composite produced by laser powder bed fusion

Understanding the microstructure and mechanical performance of heat-treated Inconel 625/TiC composite produced by laser powder bed fusion

Serena Lerda*[1,2], Giulio Marchese[1,2,3], Emilio Bassini[1,2,3], Mariangela Lombardi[1,2,3], Daniele Ugues[1,2,3], Paolo Fino[1,2,3], Sara Biamino[1,2,3]

[1]DISAT – Department of Applied Science and Technology, Politecnico di Torino, Corso Duca degli Abruzzi 24, 10129 Torino, Italy
[2]IAM@PoliTo – Interdepartmental Center of Integrated Additive Manufacturing, Politecnico di Torino, Corso Castelfidardo 51, 10129 Torino, Italy
[3]INSTM - Consorzio Interuniversitario Nazionale per la Scienza e Tecnologia dei Materiali, Via G. Giusti 9, 50121 Firenze, Italy

Corresponding author: serena.lerda@polito.it

DOI https://doi.org/10.1016/j.msea.2023.145508

Abstract

This work aims to develop and characterize Inconel 625 (IN625) reinforced with 1wt% of sub-micrometric TiC particles processed by the Laser Powder Bed Fusion (LPBF) process. The effect of TiC particles on the IN625 alloy was investigated in the as-built and two heat-treated conditions. A volumetric energy density of 99 J/mm^3 could produce bulk IN625 and IN625/TiC samples with residual porosity less than 0.15 %. The as-built IN625 and IN625/TiC showed columnar grains along the building direction and sub-micrometric dendritic architectures. The as-built IN625/TiC presented higher hardness, tensile strength, and similar elongation at failure with respect to the as-built IN625 alloy. These mechanical properties are mainly attributed to the reinforcement effect of the TiC particles predominantly located along the grain boundaries, melt pool contours, and interdendritic areas. After heat treatments at 980 °C and 1150 °C, the IN625 alloy and IN625/TiC composite presented different microstructure stability and mechanical properties evolution, revealing greater hardness and tensile strength for the composite. In particular, when heat-treated, the IN625 was subjected to a remarkable dendritic dissolution at 980 °C and recrystallization at 1150 °C. Conversely, the IN625/TiC revealed a limited dendritic dissolution at 980 °C and the inhibition of recrystallization at 1150 °C. Overall, the pinning effect of the TiC particles was effective in providing less microstructure and mechanical properties variations under heat treatments. The current work describes the effect of adding TiC particles on the microstructure stabilization and mechanical properties evolution of additively processed LPBFed IN625 alloy in as-built and heat-treated conditions.

Keywords: Ni-based superalloys; Laser Powder Bed Fusion; Inconel 625; mechanical properties; heat treatments; Titanium carbides.

1. Introduction

Ni-based superalloys are well-known as high-performance materials characterized by good mechanical performance between 540 °C and 1000 °C, also including excellent thermal fatigue, corrosion, and oxidation resistance [1,2]. For these reasons, the main applications of this class of materials are in the aerospace, chemical, and petrochemical industries [3]. The superior properties of Ni-based superalloys derive from the solution strengthening thanks to a wide range of possible alloying elements and the formation of strengthening phases occurring under heat treatments or during service at high temperatures [4–7].

However, machining these alloys is quite expensive and difficult due to their high hardness coupled with low thermal conductivity, which induces a high heat, thus reducing the life of the subtractive tools [3,8]. Hence, additive manufacturing techniques have gained considerable attention for the potential to limit subtractive manufacturing operations for fabricating complex shape components. In particular, Laser Powder Bed Fusion (LPBF) has been widely used to process Ni-based superalloys producing near-net-shape components layer-by-layer, starting from powder [9–11].

Nowadays, a considerable amount of research has focused on Ni-based superalloys processed by LPBF, and one of the most used is the Inconel 625 (IN625), thanks to its high weldability [12–14]. IN625 is a Ni-Cr-based superalloy characterized by excellent corrosion and oxidation resistance in temperatures up to around 980 °C combined with good mechanical properties up to around 650 °C. The mechanical properties can be enhanced by the formation of the metastable coherent body-centered tetragonal γ'' (Ni_3Nb) phase, which turns into the stable incoherent orthorhombic δ phase (Ni_3Nb) after prolonged thermal exposures around 650-900 °C leading to a ductility reduction. Moreover, the formation of different types of carbides, such as (Nb,Ti-rich) MC, (Mo, Cr, and Si-rich) M_6C, and (Cr-rich) $M_{23}C_6$ carbides, can play a role in strengthening the alloy [6,15,16].

In recent years, more attention has been given to producing laser powder bed fused (LPBFed) IN625 composite to enhance its performance. Considering the applications of the IN625 alloy, the development of IN625 composites can make it possible to increase its mechanical properties together with the maximum operative

service temperature for the aerospace sector, like for gas turbine blades as well as increase the hardness and wear resistance keeping high corrosion resistance for petrochemical applications [17,18].

However, one of the common key issues is to find the process parameters to generate composites with relative density compared to the base alloy. For instance, Zhang et al. [19] reported that the addition of 5wt% micrometric TiB_2 resulted in a composite with a significant increment of hardness, even if the addition of the TiB_2 generated more defects resulting in a relative density of 96.1% against the relative density of 98.3 % of the IN625 alloy. Ghodsi et al. [20] obtained IN625 with 1wt% of YSZ with a relative density of 97%, around 2.4 % lower than IN625 processed with the same energy density, indicating the necessity to use different parameters. In fact, by applying high energy parameters, they achieved a composite with a relative density of 99 %. They showed that the sub-micrometric YSZ acted as a nucleation site during the solidification step leading to a refined microstructure and hardness increment of 30% compared with the IN625 alloy. Cooper et al. [21] investigated the addition of 5 wt% of SiC, Al_2O_3, and TiC particles into the IN625 alloy. They reported that IN625/SiC and IN625/Al_2O_3 composites presented a large number of defects. Differently, they underlined the positive effect of using TiC particles in the IN625 matrix. IN625/TiC composite was successfully processed without microcracks, and an appreciable increase in hardness value was observed. This could be attributed to the smaller particle sizes as well as the good weldability and chemical stability in Ni-based superalloys [22].

Due to the attractive characteristics of the TiC particles, several studies paid attention to the development and characterization of IN625/TiC composites processed by directed energy deposition (DED), another laser additive manufacturing process [23–28]. However, only a few published papers deal with the microstructure and mechanical performance of IN625/TiC composite processed by LPBF.

Regarding the LPBFed IN625/TiC composites, Chen et al. [22] studied the as-built IN625 reinforced with 4wt % of nanoTiC particles revealing that high energy density must be applied to obtain dense composites with with small pores. They also showed that the composite presented higher tensile strength due to Orowan strengthening, dislocation density, grain size refinement, and lead-bearing transformation induced by the TiC particles. Chen et al. [29] also investigated the IN625/TiC with 6 wt% of nano TiC reporting higher microhardness and wear resistance with respect to the base alloy. In another work, Chen et al. [30] showed that the composite with 4wt% of nanoTiC presented higher oxidation resistance compared to the IN625 alloy

in heat-treated conditions. In a previous work of our research group, IN625 reinforced with 1wt% of micrometric TiC particles exhibited superior thermal stability, showing that the columnar grains structures remained stable for a solution annealing performed at 1150 °C for 2 hours [31]. Also, in this case, more energetic process parameters must be employed to generate a dense composite, and the addition of micrometric TiC particles generated a limited hardness increment of around 6 % compared to the as-built IN625 alloy. All these studies underline the advantages of adding TiC particles as reinforcement to the IN625 matrix.

Although there are already a few studies on the microstructure and mechanical properties of as-built LPBFed IN625/TiC composite, there is still need to shed light on its microstructure and mechanical properties evolution under heat treatments. To the authors' knowledge, no studies have focused on the correlation of the microstructure with the mechanical properties of both as-built and heat-treated LPBFed IN625/TiC composites.

The current study shows a process parameter optimization on IN625 with 1wt% of sub-micrometric TiC particles compared to the IN625 alloy. In addition, the microstructure, degree of recrystallization, hardness, and tensile properties were evaluated in as-built and heat-treated conditions. The results underlined the beneficial effect of adding sub-micrometric TiC particles on mechanical performance. Furthermore, the TiC particles help to hinder the recrystallization and grain growth under heat treatments at high temperatures, thus resulting in mechanical properties more similar to the as-built condition compared to the heat-treated IN625 alloy.

2. Materials and methods

2.1 Powder characterization

The gas-atomized IN625 powder, used as base alloy and metal matrix, was purchased by EOS GmbH (Krailling/Munich, Germany) with a given D_{50} of around 35 μm. The chemical composition of IN625 powder and its morphology were analyzed by means of a focused ion beam scanning electron microscope (FIB-SEM, TESCAN S9000G, Tescan Company, Brno, Czech Republic) equipped with an energy dispersive spectroscopy (EDS) system. Moreover, the C content was determined by means of a LECO detector (LECO, CS 744 LECO-

analyser, Leco, St. Joseph, MI, USA). The evaluated chemical composition (**Table 1**) complied with the range reported in the UNS N06625 standard.

The IN625 powder mainly consisted of almost spherical particles (**Fig. 1** (a)) with dendritic surfaces generated by the high cooling rate of the gas-atomization process (**Fig. 1** (b)). TiC particles, used as ceramic reinforcement, were supplied by Sigma-Aldrich (Merck KGaA, Darmstadt, Germany) with a given average granulometry of 200 nm.

The IN625 powder was mechanically mixed with 1wt % of TiC particles in jars for 24 hours without grinding medium, applying a speed rate of 60 rpm. The SEM micrographs underline that the TiC particles covered the surface of the IN625 powder, as displayed in **Fig. 1** (c and d). Some TiC aggregations with dimensions above 200 nm could be detected after the mixing due to the Van der Waals forces acting on sub-micrometric particles, as depicted in EDS maps in **Fig. 1** (e).

Table 1 Chemical composition (in wt.%) of IN625 evaluated with EDS and LECO combustion analysis.

Ni	**Cr**	**Mo**	**Fe**	**Nb**	**Co**	**Si**	**Ti**	**Al**	**C**
Bal.	22.4	8.4	0.9	3.5	0.5	0.2	0.3	0.2	0.020

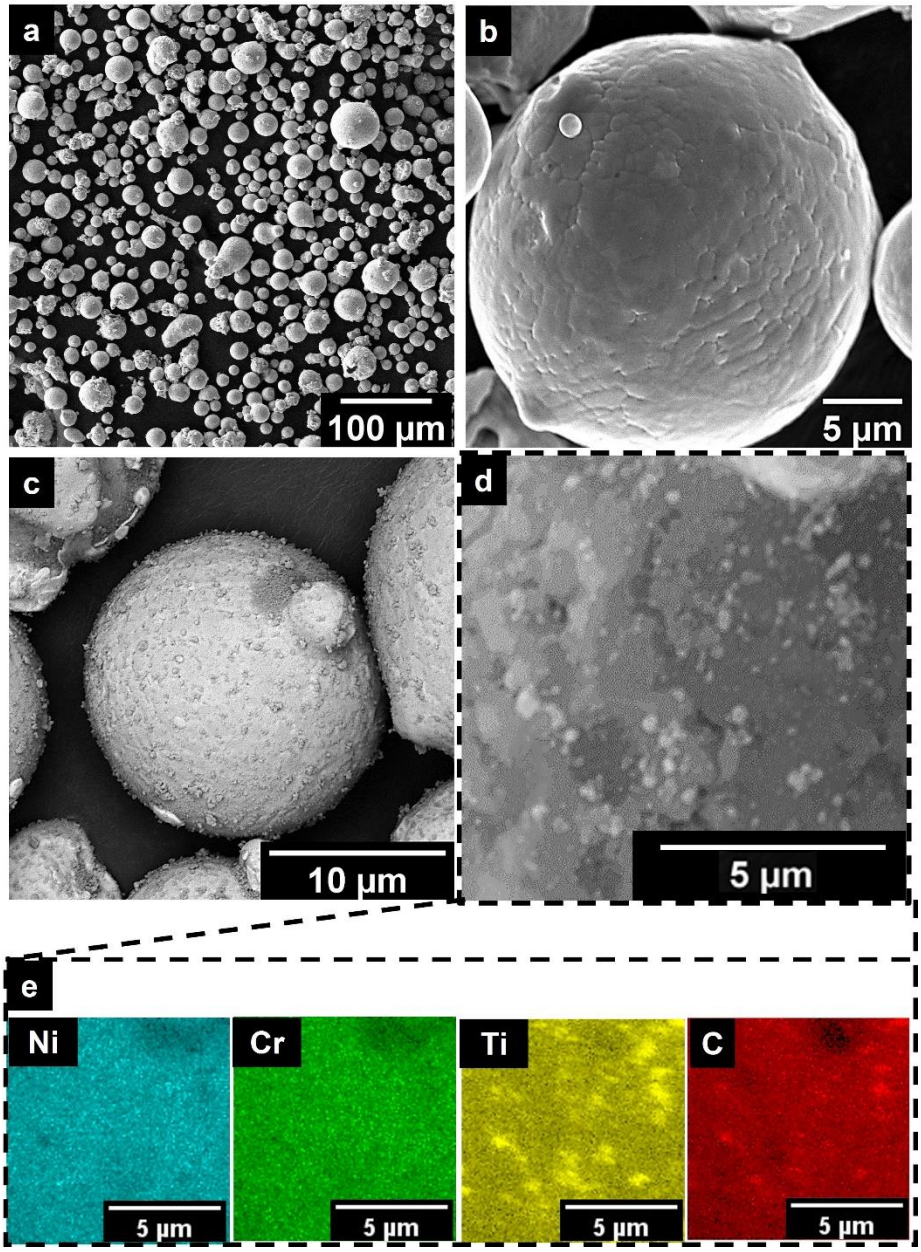

Fig. 1. (a,b) SEM image of IN625 particles at different magnifications; (c,d) SEM images of IN625/TiC at different magnifications showing the IN625 particle surface decorated with TiC particles. (e) EDS maps of the Ni, Cr, Ti, and C on one IN625 particle surface, showing the presence of TiC particles.

Before processing, the two powders, IN625 and IN625/TiC were sieved below 50 µm, and a flowability test was carried out with the Carney flowmeter funnel following the ASTM B964. The flowability of the composite powder presented a slightly lower value than the base alloy, but a superior flow rate to the IN625/TiC with micrometric size, as reported in **Table 2.** A significant reduction of the flowability could result in the formation of a non-homogenous layer of powder during the LPBF process, bringing to defects formation. It should be noted that the Carney Flowmeter funnel was used since the powder did not flow in the Hall Flowmeter funnel.

Table 2 IN625 and IN625/TiC flowability result

Powder	Carney flow rate [s/150g]
IN625	8.7 ± 0.1
IN625/TiC sub-micrometric	11.8 ± 0.3
IN625/TiC micrometric [31]	14.5 ± 0.5

2.2 LPBF process

The IN625/TiC mixed powder and IN625 powder were processed by means of an MLab Cusing R Machine (Concept Laser GmbH, Lichtenfels, Germany) exploiting a maximum 100 W power fiber laser with a spot size of around 50 μm. In this study, laser power, hatching distance, and layer thickness were fixed at values equal to 95 W, 0.04 mm, and 0.02 mm, respectively. Several scanning speeds were investigated: 1600, 1200, 1000, 800, and 600 mm/s in order to determine the optimized set of building parameters. The previously mentioned process parameters combination corresponds to five volumetric energy densities (VEDs) of 74, 99, 119, 148, and 198 J/mm^3. Cubes (10 mm x 10 mm x 10 mm) and tensile specimens (gauge length of 16 mm and diameter of 4 mm following the ASTM E8/E8M-22) were realized with a scanning strategy of 5 mm stripes and 67° rotation between each layer. No pre-heating temperature was applied to the building platform.

2.3 Heat treatments

In order to investigate the microstructure evolution under heat treatments, two typical heat treatments of the IN625 alloy were performed on the as-built (hereafter AB) IN625 and IN625/TiC specimens [7,32]. The heat treatments were followed by water quenching in order to avoid microstructure changes during the cooling stage. In particular, the annealing treatment (abbreviated as HT1) was carried out at 980 °C for 1 hour, while the solution annealing treatment (abbreviated as HT2) was performed at 1150 °C for 2 hours. The HT1 is in the range of temperature considered as Grade 1, while the HT2 temperature is associated with a Grade 2 condition, based on the ASTM B446.

2.4 Microstructure and mechanical characterizations

The AB and HT IN625 and IN625/TiC samples were cut along the building direction (z), grounded with SiC papers, and subsequently polished with 1 μm diamond suspension. Porosity evaluation was performed on the polished samples using a Light Optical Microscope (Leica DMI5000M, Wetzlar, Germany). For the analysis,

50 LOM images were taken at 500x magnification covering 1.5 mm^2, and then post-processed with ImageJ software. The polished samples were then etched with mixed acids solution (nitric acid and hydrochloric acid 1:3) in order to reveal the microstructure.

Microstructural analysis was performed by means of LOM, SEM (Phenom XL), and FIB-SEM (TESCAN S9000G) equipped with electron backscattered diffraction (EBSD) and flight secondary ion mass spectroscopy (Tof-SIMS) detectors. For EBSD and Tof-SIMS analyses, an additional polishing step was carried out on samples with colloidal silica suspension (0.04 μm). EBSD analysis was performed using a tilting angle of 70° and scanned at 20 kV and 10 nA using a step size of around 2 μm while the Tof-SIMS analyses were performed on samples tilted at 55° using 30 kV and 1 nA. In order to study the level of microstructure stabilization of the alloy and composite under heat treatments, the grain orientation spread (GOS) was used to determine the fraction of recrystallized grains. The GOS value is the average misorientation angle between each analyzed point inside the grain and the average grain orientation. Based on the literature, recrystallized grains presented very lower dislocation density, while the deformed ones are characterized by high dislocation density. The typical threshold to consider a grain as recrystallized grain can be fixed at 2° [33–37].

Moreover, X-ray diffraction (XRD) analyses were performed utilizing an Empyrean diffractometer (PANalytical, Almelo, The Netherlands) using CuKα radiation and a Bragg Brentano configuration. The analysis was performed from 20 to 100° with a step size of 0.013° and a detection time of 25 s for each step. In order to evaluate the gamma (γ) and carbides lattice parameter, Bragg's law Eq (1) was used. Where λ is the wavelength of the radiation used, $d_{h,k,l}$ is the interplanar distance, and θ is the XRD angle of the peak considered. The lattice parameter (a) was calculated considering Eq (2), where h, k, and l are the miller index of the crystallographic plane associated with the considered peak [38].

$$2d_{hkl}\,sin\,\theta = n\lambda \quad (1)$$

$$a = d_{hkl}\sqrt{h^2 + k^2 + l^2} \quad (2)$$

Furthermore, to better evaluate the lattice constant of the γ matrix, the Nelson – Riley method was applied considering the (111), (200), (220), (311), and (222) peaks. The lattice parameter was plotted with the Nelson – Riley coefficient Eq (3) and then fitted. The intercept was considered a lattice constant [39].

$$Nelson - Riley\ coefficient\ = \frac{1}{2}\left(\frac{(\cos\vartheta)^2}{\sin\vartheta} + \frac{(\cos\vartheta)^2}{\vartheta}\right) \quad (3)$$

Finally, Brinell hardness and tensile tests were carried out on IN625 and IN625/TiC in the AB and HT conditions. The first test was conducted with an EMCO TEST M4U durometer (EMCO-TEST Prüfmaschinen GmbH, Kuchl, Austria) in HBW2.5/62.5 condition following the ATSM 10. Ten indentations were performed on each tested sample. Tensile tests were performed on three specimens for each condition for both alloy and composite utilizing a Zwick-Roell all-around Line Z050 (Zwick-Roell Materials Testing, Genova, Italia) equipped with an extensometer, applying a deformation rate of 0.128 mm/s using an extensometer. The tensile specimens were built perpendicular to the building direction along the xy plane, with a gauge length of 16 mm and diameter of 4 mm following the ASTM E8/E8M-22. The strain hardening ability was calculated to better understand the behavior of both IN625 and IN625/TiC composite during plastic deformation by means of the Ludwik method [40,41]. This method considers the plastic deformation from the yield strength to the ultimate tensile strength, and it was demonstrated to be precise for determining the strain hardening for the Ni-based superalloys [40]. The Ludwik model can be written as the following Eq (4):

$$\sigma = \sigma_Y + K(\varepsilon - \varepsilon_Y)^n \quad (4)$$

Where n is the hardening exponent, K is the strength parameter of the superalloy, σ and σ_Y are the true and yield stress, respectively; ϵ and ϵ_Y are the true strain and the elongation at yield, respectively.

3. Results and Discussion

3.1 LPBF parameters optimization

Fig. 2 (a) shows the residual porosity of IN625 and IN625/TiC composite fabricated using different process parameters, while representative LOM images are displayed in **Fig. 2** (b). Using a VED of 74 J/mm^3, both alloy and composite samples showed lack of fusion defects and circular pores (**Fig. 2**(b)), resulting in a porosity level between 0.40% and 0.25%. Increasing the VED at 99 J/mm^3, only circular pores could be detected (**Fig. 2** (b)), leading to a porosity below 0.15 %. Upon further increment of VEDs, the porosity gradually decreased, reaching values less than 0.10 % for a VED of 198 J/mm^3 for the alloy and the composite (**Fig. 2** (b)).

Since a VED of 99 J/mm^3 guaranteed a residual porosity below 0.15 % combined with a good building time, this value was selected as the optimized one for the production of IN625 and IN625/TiC samples.

In order to obtain adequate densification, the influence of the surface tension, viscosity, and convective motion (Marangoni flow) of the liquid during the melting stage should be considered [42–44]. The presence of the TiC particles can increase the viscosity and reduce the surface tension of the liquid into the melt pool, thus limiting the motion and spreading of the liquid resulting in the formation of defects, like the lack of fusion denoted in the samples processed with VED 74 J/mm^3. In this case, high energetic parameters must be applied to obtain high temperatures in the melt pools, thus inducing high surface tension and low viscosity in the formed liquid, acting as a driving force for liquid spreading into the melt pool, as observed for VED $\geq$ 99 J/mm^3.

The Marangoni flow provides the mixing of the TiC particles into the metal liquid. The TiC presents higher laser absorptivity and thermal conductivity than IN625 alloy, and consequently, the mixed composite powder is characterized by higher temperatures in the melt pool compared to the IN625 alloy, as observed by Lee et al. [23], which produced IN625/TiC by DED process.

Therefore, it is possible to infer that the high temperature inside the melt pool partially dissolved the TiC particles that precipitate in TiC or other MC carbides during the solidification inside the interdendritic zones or grain boundaries enriched in C and other segregated chemical elements like Ti and Nb.

However, the gradient temperature within the melt pool involved the generation of zones with different temperatures, as also highlighted by studies of melt pool dynamics on the LPBFed materials [45]. Consequently, a part of the TiC particles could remain unmelted, and during the solidification, these carbides could be pushed to the grain boundaries and melt pool contours. This scenario could also explain the few TiC segregations observed during the microstructure investigation.

Finally, the microstructure analysis revealed that the unmelted TiC particles in the molten melt pool did not significantly reduce the liquid viscosity since the specimens exhibited a high densification level with a residual porosity similar to the IN625 alloy processed with the same parameters.

This can be attributed to the low concentration of reinforced TiC particles, while a higher quantity could cause alterations in increasing the melt pool viscosity during the melting process. A similar effect was observed by Chen et al. [22] that reported that more energetic parameters (VED of 208 J/mm^3) were necessary to produce IN625 with 4wt% nanoTiC to reach high densification level.

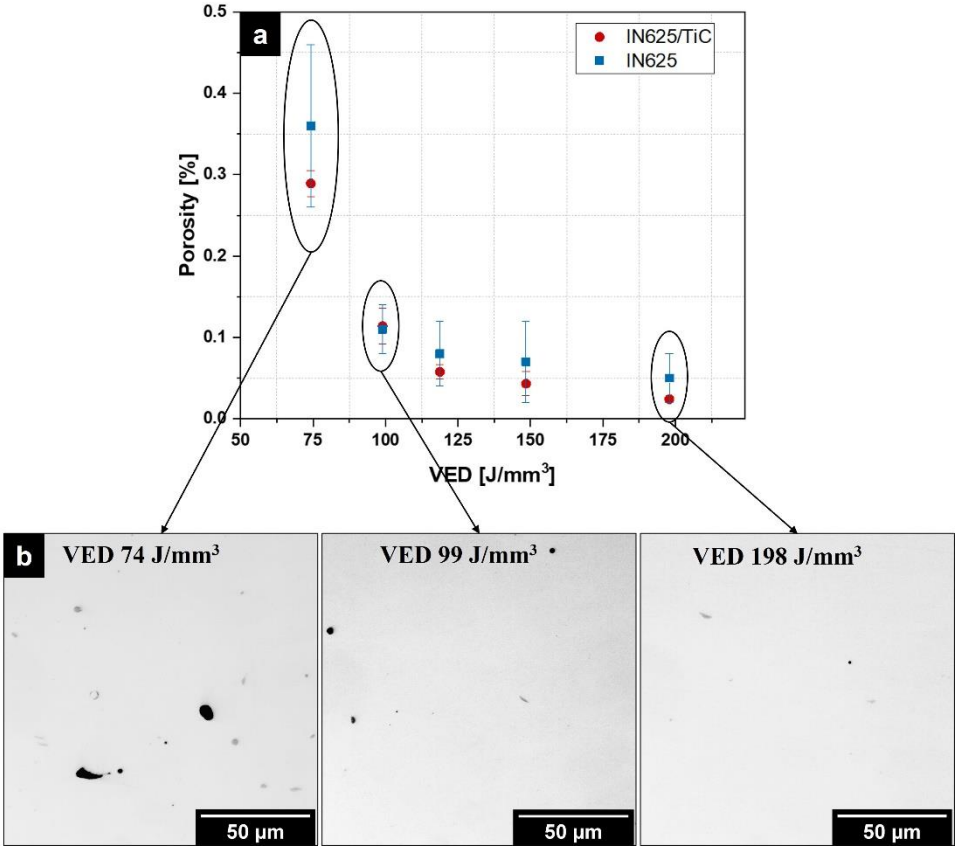

Fig. 2. (a) Porosity evolution at increasing VED for IN625 and IN625/TiC samples; (b) LOM images of the polished IN625/TiC composite built using VED at 74 J/mm^3, 99 J/mm^3, and 198 J/mm^3.

3.2 Recrystallization evolution under heat treatments

The EBSD GOS maps and the GOS, HAGBs, and LAGBs distributions are displayed in **Fig. 3** (a), (b), (c), and (d). Moreover, the IPF YO maps and the respective pole figure are given in Appendix A.

The AB IN625 and IN625/TiC showed a very high fraction of columnar deformed grains (around 80 %) and a low fraction of recrystallized grains (around 20 %) due to the high residual stresses accumulated during the LPBF process. The AB alloy and AB composite presented similar concentrations of LAGBs around 50 %, thus indicating a similar level of dislocation density. For the AB IN625, the recrystallized grains appeared to be concentrated in some areas and to follow the melt pool contours. In fact, the remelting process can also partially

release the residual stresses, thus forming the recrystallized grains in these areas. On the other hand, the AB IN625/TiC showed recrystallized grains more homogenous scattered throughout the material, which could derive from the grain refinement caused by the added TiC particles. In the literature, more intense grain refinement was observed for IN625/TiC composite processed with a higher concentration of TiC [22]. Regarding the grain sizes, the composite presented columnar grains with lengths from 20 µm to 370 µm and widths of 20 µm and 40 µm against the AB IN625 alloy with columnar grains with lengths ranging from 20 µm to 400 µm and widths from 20 µm to 50 µm. Moreover, a population of small equiaxed grains with average dimensions of around 6 µm could be detected in both cases.

After HT1, IN625 and IN625/TiC did not show recrystallization phenomena (deformed grains remained around 80 %) for both alloy and composite, as also depicted by the trend of the GOS angle in **Fig. 3** (b and c). The HT1 IN625 alloy showed a slight reduction of the LAGBs compared to the AB IN625 alloy, while the HT1 IN625/TiC presented LAGBs similar to the AB IN625/TiC condition, as denoted in **Fig. 3** (d). The slight reduction in LAGBs of the IN625 alloy could derive from the initial dendritic dissolution, while for the composite, the TiC limited the dendritic dissolution, thus generating a reduced LAGBs variation. The average dimensions of the grains remained in the range of the respective AB conditions. The literature on LPBFed IN625 agrees with the current results indicating that a more elevated temperature is necessary to trigger recrystallization [46,47].

Finally, the HT2 IN625 was subjected to full recrystallization with the release of the residual stresses and the formation of recrystallized equiaxed grains (96 %) and a limited fraction of deformed grains (4 %). On the contrary, the recrystallization was inhibited for the IN625/TiC composite, thus showing a GOS trend similar to the AB and HT1 IN625/TiC composite (**Fig. 3** (b and c)). The distribution of LAGBs and HAGBs (**Fig. 3** (d)), showed the almost elimination of LAGBs for the alloy while the composite still presented a condition close to the AB and HT1 IN625/TiC conditions (**Fig. 3** (d)). After HT2, the base alloy presented equiaxed grains with mean sizes of around 60 µm, including some smaller grains with a minimal size of around 10 µm and larger grains up to around 180 µm. The HT2 IN625/TiC composite still presented columnar grains with lengths ranging from 20 to 500 µm and widths between 5 and 70 µm, thus suggesting a limited grains coarsening with respect to the AB IN625/TiC state. Interestingly, some small equiaxed grains could be

observed in the composite, and the mean size was around 6 µm. These small grains presented the same dimensions as those observed in the AB IN625/TiC condition, indicating that these small grains survived under the high temperature of the solution annealing treatment.

The combined analysis of the GOS, HAGBs, and LAGBs with the grain dimensions of the AB and HT conditions indicated that the TiC particles generated a significant pinning effect on the grain boundaries as well as the sub-structures, thus keeping the original columnar grains of the AB condition.

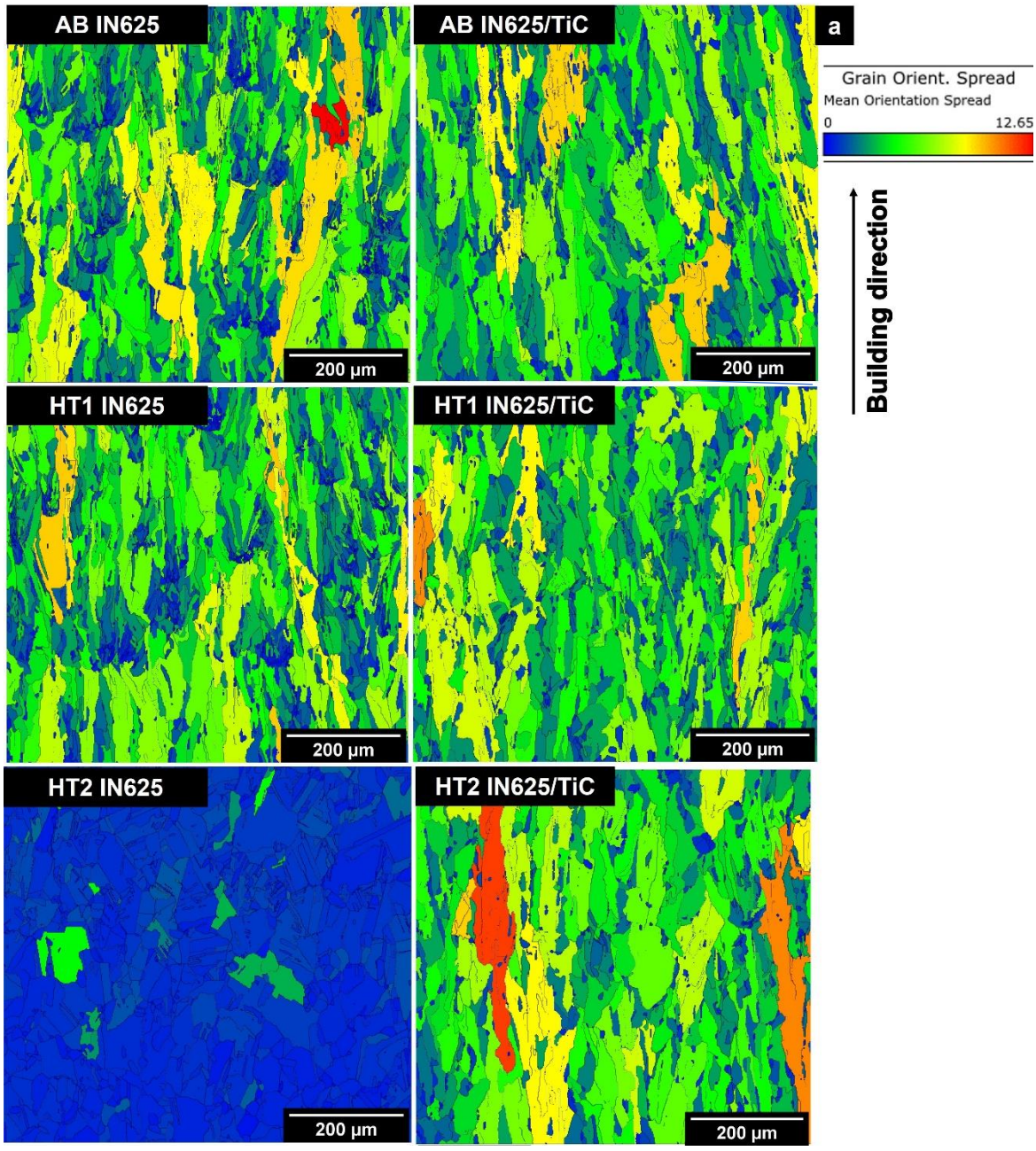

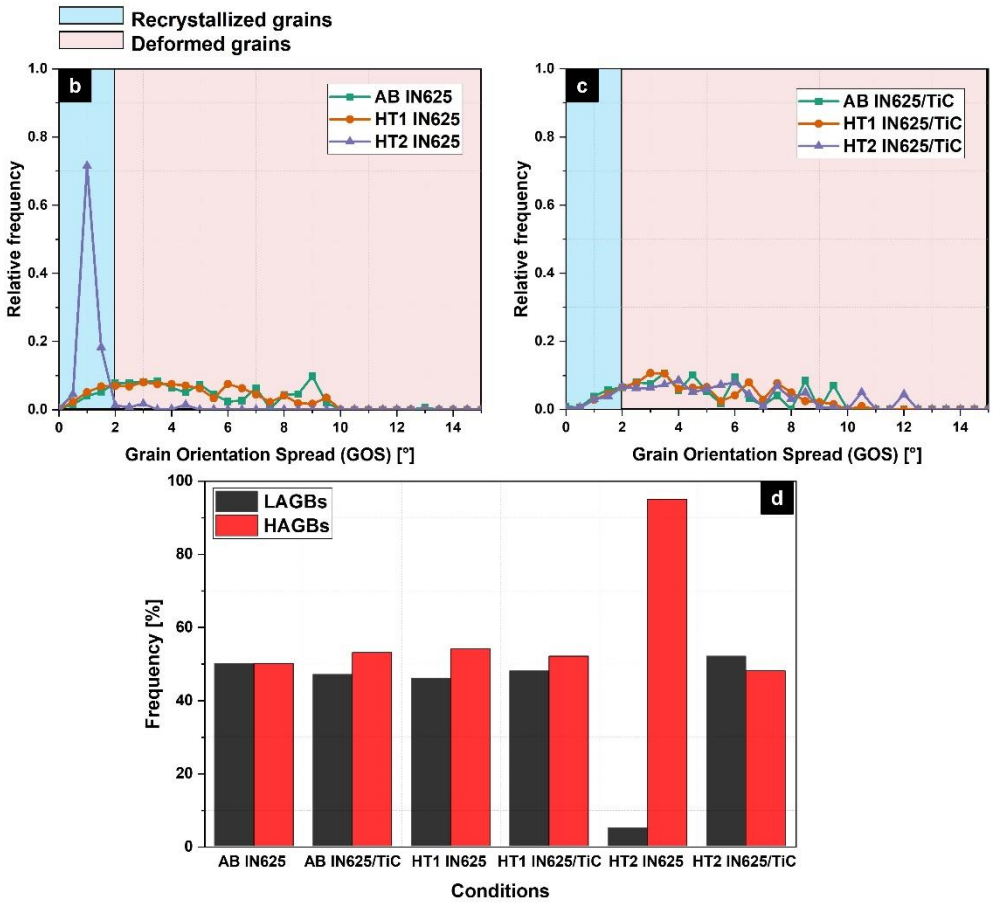

Fig. 3 (a) EBSD GOS maps of IN625 and IN625/TiC in the AB and HT conditions along the building direction. The HAGBs are indicated by black lines. (b) IN625 and (c) IN625/TiC relative frequency of GOS results. (d) HAGBs (10-60°) and LAGBs (2-10°) frequency of the IN625 and IN625/TiC samples.

3.3 Microstructure evaluation

3.3.1 As-built condition

IN625 and IN625/TiC composite in AB condition exhibited columnar grains parallel to the building direction and the melt pools, as visible in LOM images reported respectively in **Fig. 4** (a) and (b). In addition, SEM images (**Fig. 4** (c) and (d)) revealed a fine dendritic microstructure in both base alloy and composite. The sub-micrometric size of the dendritic architectures is caused by the high cooling rates of the LPBF process, up to around 10^6 K/s [48].

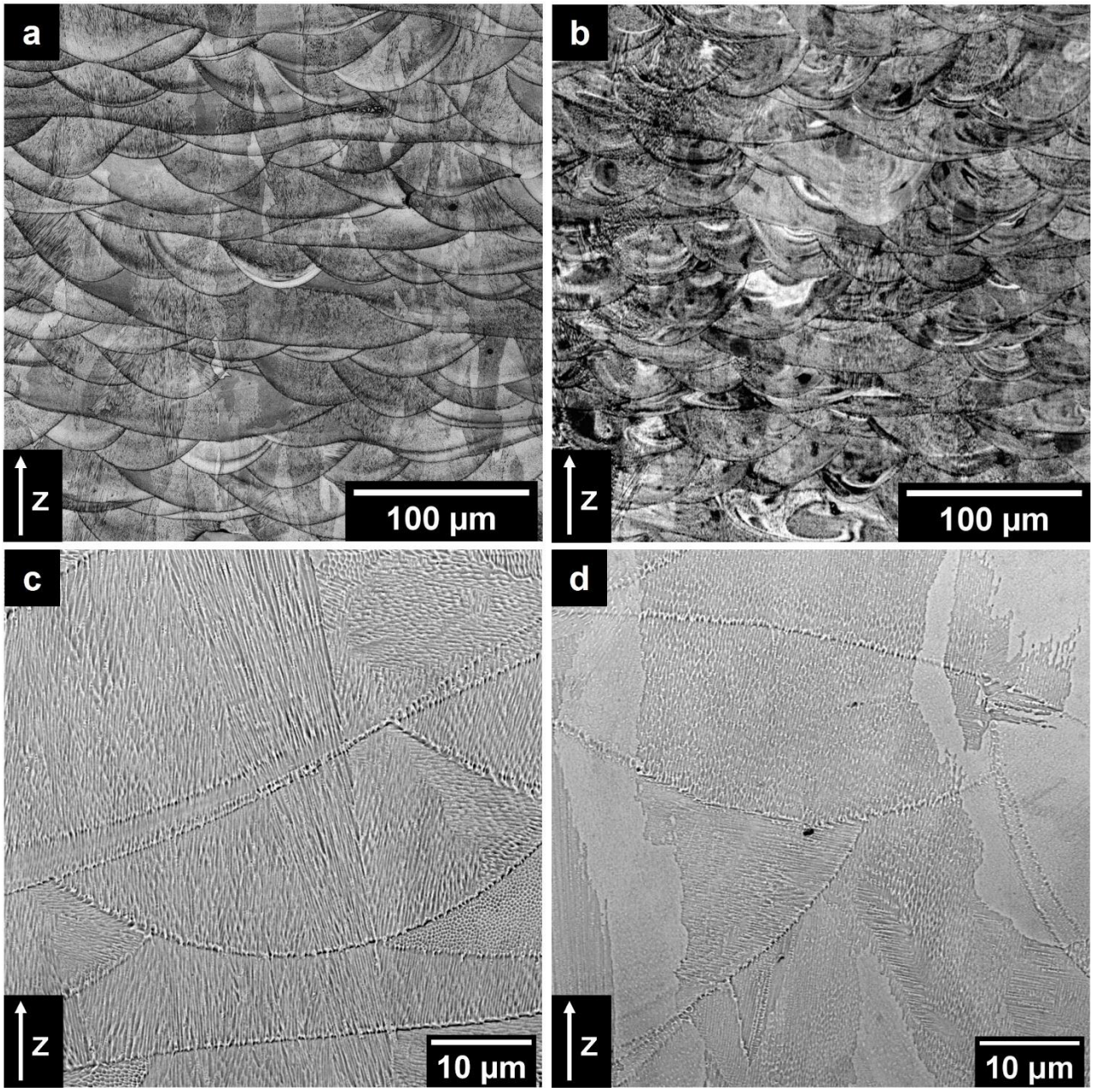

Fig. 4 LOM images of the AB condition of IN625 (a) and IN625/TiC (b); SEM images of IN625 (c) and IN625/TiC (d). The samples are chemically etched.

Focusing on the composite, the TiC particles can be found chiefly located along the grain boundaries, as observed in the EBSD phase map in **Fig. 5** (a), where the presence of TiC is pointed out in green and the γ matrix in red. Moreover, IN625/TiC showed some isolated micro-segregations of TiC located mainly along the melt pool boundaries, as visible from the SEM-EDS analysis in **Fig. 5** (b). The possible origin of the micro-segregations was explained in detail in the 3.1 paragraph.

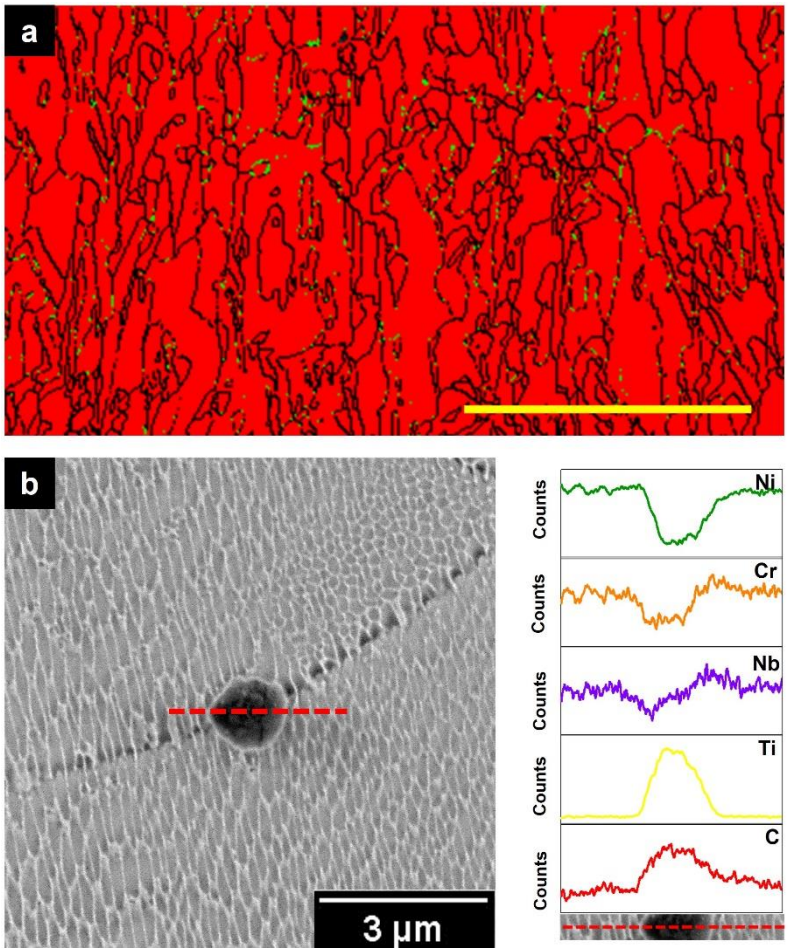

Fig. 5 (a) EBSD phase maps with Ni-based superalloy in red and TiC phase in green. The high-angle grain boundaries are highlighted in black. The marker is 200 µm. (b) SEM-EDS line on micro-segregations of TiC at the melt pool boundary for the AB IN625/TiC sample.

The IN625 and IN625/TiC samples were also analyzed by means of Tof-SIMS analysis, as displayed in **Fig. 6**. The IN625 alloy showed a partial enrichment of Nb along the melt pool boundaries and interdendritic areas (pointed by the yellow arrow), while Ti was found mainly concentrated along the interdendritic areas. This result is in agreement with the solidification of the IN625 alloy, where segregations of Nb and Ti tend to be located in the interdendritic areas [12,49]. Likewise, observing the AB IN625/TiC condition, enriched areas of Nb were found in correspondence to melt pool boundaries (highlighted by the yellow arrow) and interdendritic areas. Moreover, in the case of Ti, a higher concentration can be detected along the melt pool contours and in the interdendritic areas, indicating that the TiC particles tend to be located in these areas during the solidification.

Overall, the combination of EBSD, SEM-EDS, and Tof-SIMS analyses revealed that the TiC particles were mainly located in the grain boundaries, melt pool contours, and interdendritic structures.

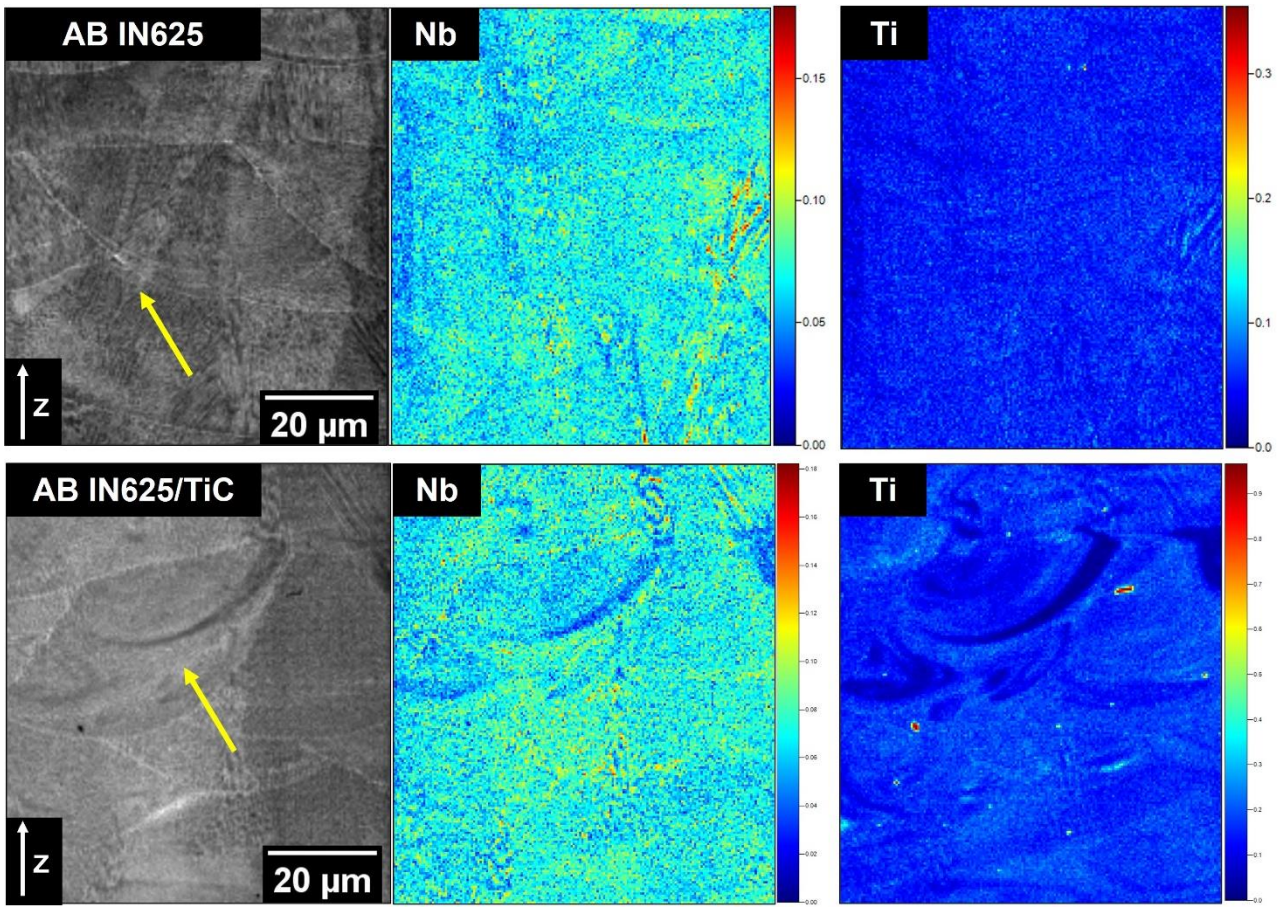

Fig. 6 Tof-SIMS maps for IN625 and IN625/TiC in the AB condition, showing the concentration distribution of Nb and Ti. Yellow arrows underlined some melt pool boundaries.

3.3.2 Heat-treated conditions

The HT1 IN625 condition (**Fig. 7** (a)) presented a more intense dissolution of the dendritic and melt pool structures compared to the HT1 IN625/TiC condition (**Fig. 7** (b)). SEM images, reported in **Fig. 7** (c) and (d), pointed out the precipitation of carbides in both base alloy and composite. EDS analyses on the precipitates showed enrichment of Nb and C correlated with depletion of Ni and Cr in the base alloy (**Fig. 8** (a)) and the composite (**Fig. 8** (b)).

A similar result indicated the formation of carbides, most likely MC carbides, based on the time-temperature-transformation (TTT) diagram of the IN625 alloy [6]. Through the SEM observations, the carbides were less abundant in IN625/TiC. HT1 IN625 developed carbides with globular and elongated shapes ranging from 1.5 to 0.3 µm. The HT1 IN625/TiC showed preferentially globular carbides with sizes between 0.6 µm and 0.2

μm. This behavior may be associated with the higher stability of the dendritic structures of the composite, thus reducing the chemical elements for the precipitation of new phases. Even in these conditions, MC can precipitate thanks to the greater driving force for precipitation under thermal exposures [50]. On the other hand, the alloy underwent a more intense dissolution of the dendritic structures leading to higher chemical element concentrations for carbide formations.

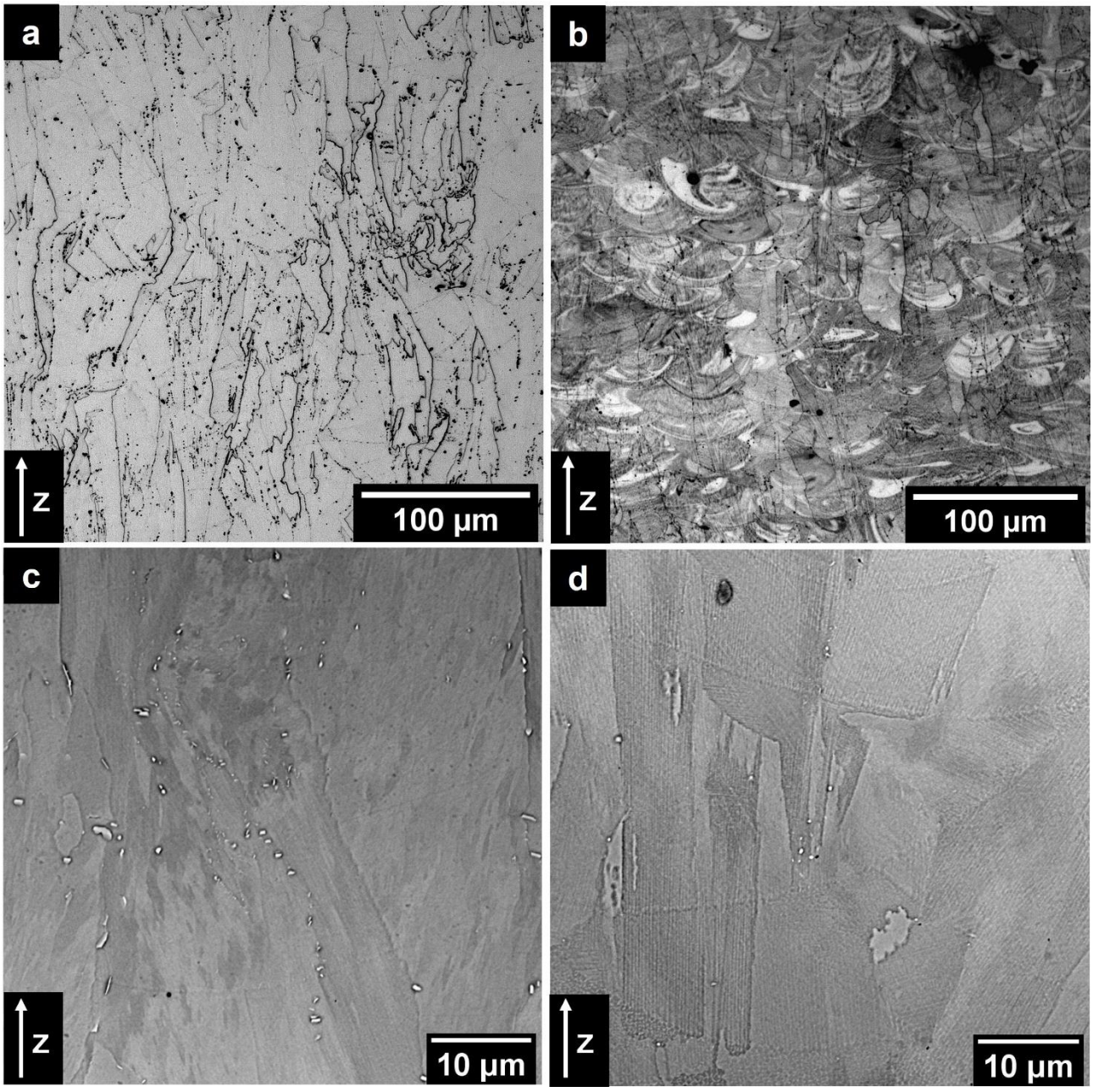

Fig. 7. LOM images of HT1 condition of IN625 (a) and IN625/TiC (b); SEM images of IN625 (c) and IN625/TiC (d). The samples are chemically etched.

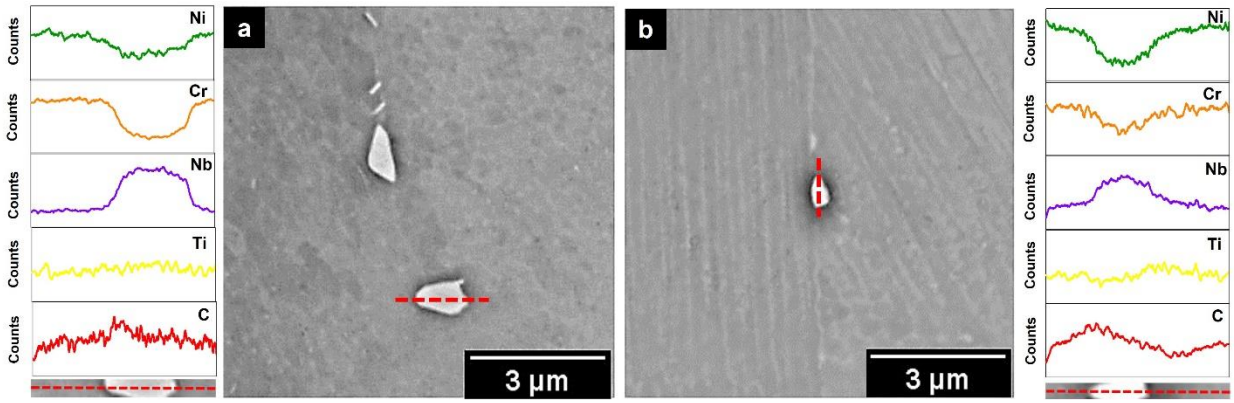

Fig. 8 SEM-EDS analysis of precipitates in HT1 IN625 (a) and HT1 IN625/TiC (b) after chemical etching.

By comparing the LOM micrographs of the HT2 condition of the IN625 and IN625/TiC (**Fig. 9** (a) and (b)), it is visible the stabilizing effect of the TiC particle on the IN625.

The composite still showed columnar grains and reshuffling in correspondence to the melt pools, whereas the recrystallization occurred in the base alloy generating equiaxial and twin grains. SEM images revealed very small carbides for the IN625 alloy (**Fig. 9** (c)), while the IN625/TiC exhibited sub-micrometric and micrometric carbides (**Fig. 9** (d)). EDS analysis on HT2 IN625/TiC precipitates revealed enrichment of Nb, Ti, and C correlated with a depletion of Ni and Cr (**Fig. 9** (e)), which can be associated with MC carbides [32].

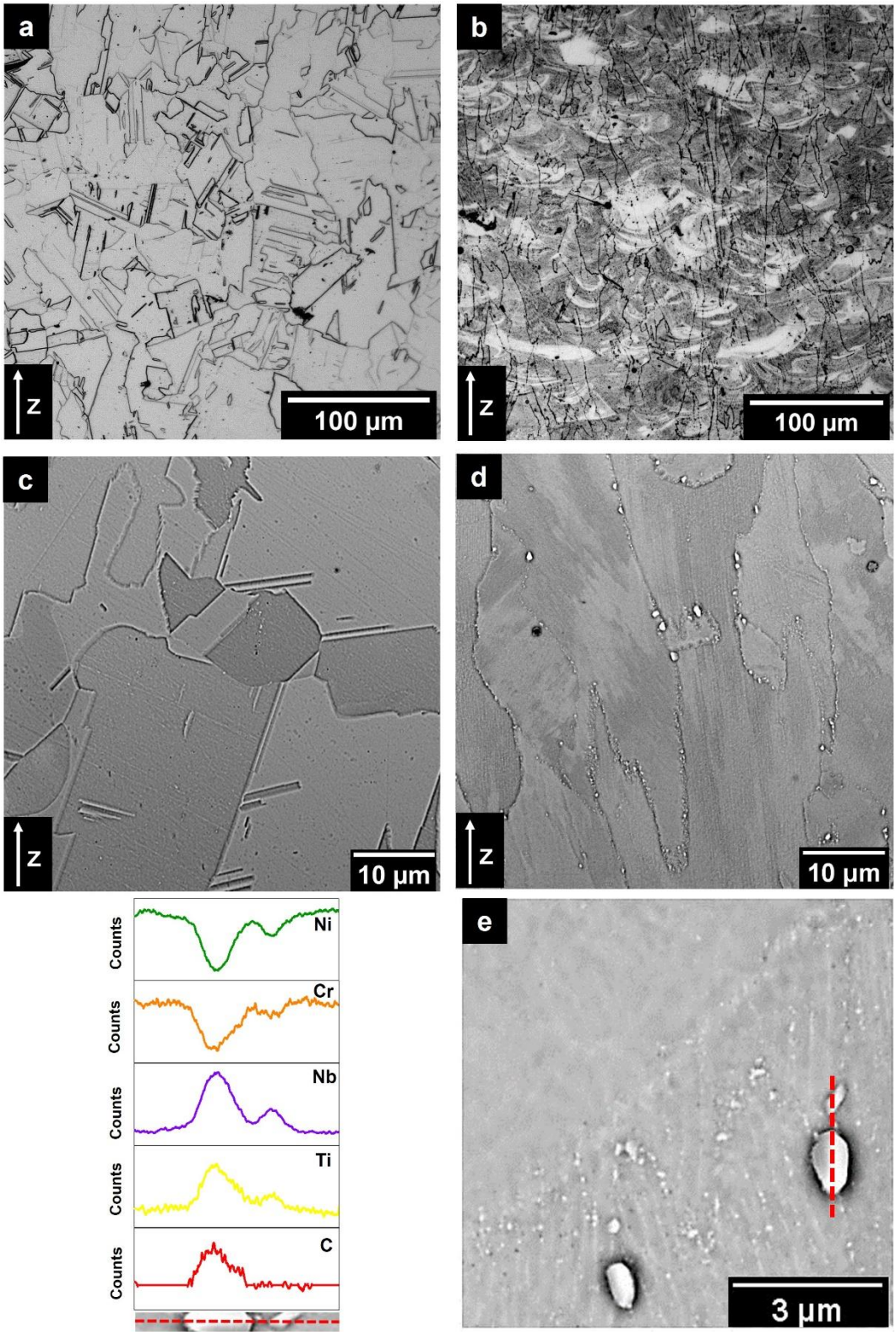

Fig. 9. LOM images of HT2 condition of IN625 (a) and IN625/TiC (b) and SEM images of IN625 (c) and IN625/TiC (d) with SEM-EDS analysis on some carbides (e). The samples are chemically etched.

From the Tof-SIMS maps (**Fig. 10**), Nb,Ti-rich MC carbides precipitate with smaller dimensions in the HT2 IN625 alloy compared to the HT2 IN625/TiC, as pointed out by the spot with high Ti and Nb concentrations.

The formation of Nb,Ti-rich MC carbides for the HT2 IN625 conditions were also observed in a previous work of some of the authors [49]. Moreover, the formation of MC carbides at 1150 °C is in agreement with TTT curves of the IN625 alloy [51]. In the HT2 IN625/TiC condition, the largest Nb,Ti-rich MC carbides were formed along the grain boundaries due to the high segregations of Nb and Ti in these areas.

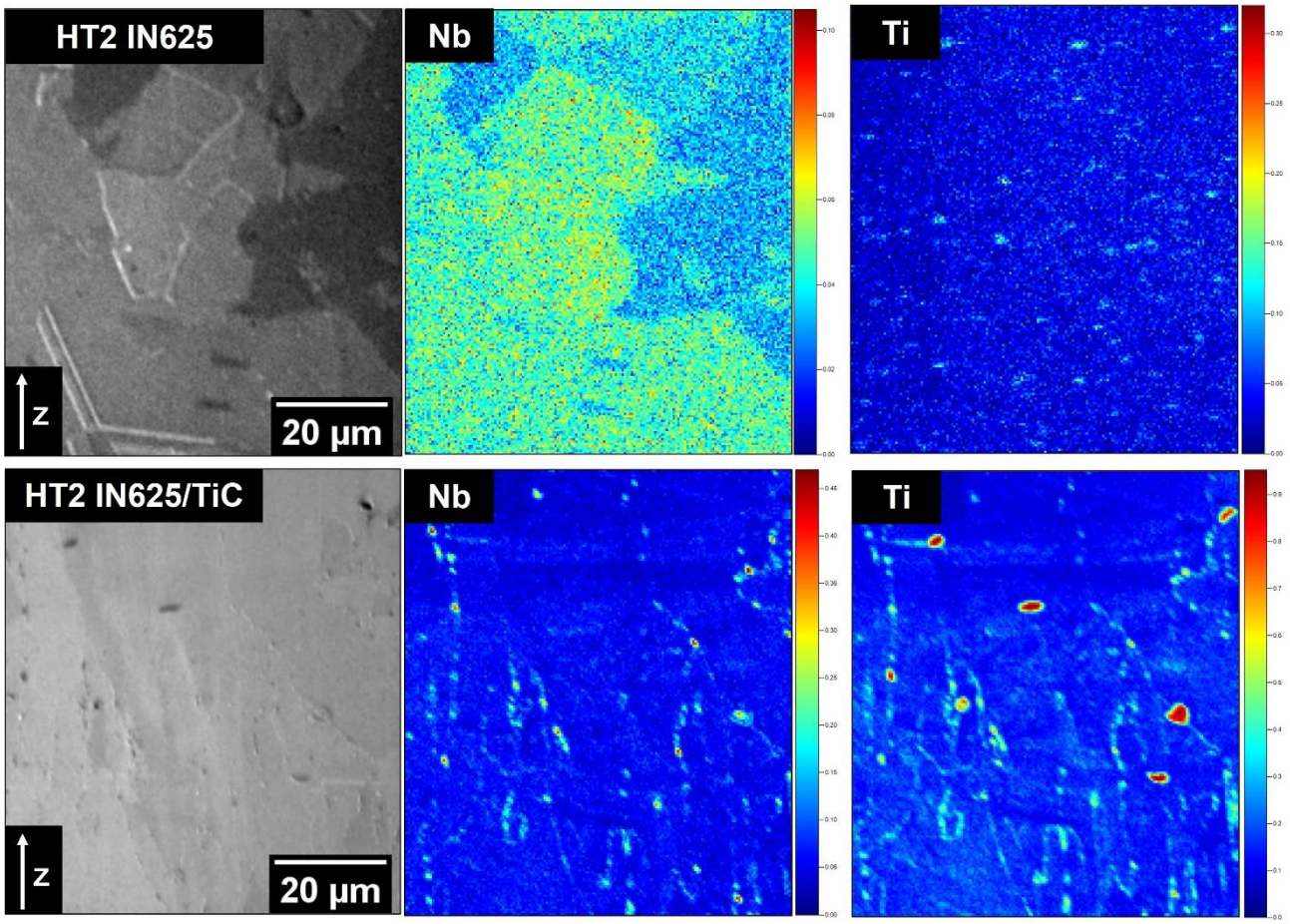

Fig. 10 Tof-SIMS maps for IN625 and IN625/TiC in HT2 condition, showing the concentration distribution of Nb and Ti

3.4 XRD analysis

The XRD patterns of the IN625 and IN625/TiC samples show the γ matrix, as provided in **Fig. 11** (a). The XRD patterns showed a strong intense peak in correspondence of the (200) plane for all the conditions, except for the HT2 IN625 state. This feature was related to the epitaxial and anisotropic grain growth in the LPBF process [22,31]. On the other hand, HT2 IN625 matched the conventional γ spectrum with the most intense peak pointed out on the (111) plane due to the recrystallization induced by the solution annealing.

For the AB and HT1 IN625/TiC composite, the added TiC particles were identified in the zoom displayed in **Fig. 11** (b), showing two peaks related to the (111) and (200) peaks identified by a triangle. The calculated

lattice parameter of the TiC particles is 0.4330 nm, which is compatible with the values reported in the literature [52]. HT2 IN625/TiC showed a shift towards smaller angles that could be correlated with the formation of new Nb,Ti-rich MC carbides, pointed out by a square. The Nb,Ti-rich MC carbides presented a lattice parameter of 0.4371 nm, consistent with the literature [7]. It should be noted that the peaks of the formed MC carbides could not be detected in the HT1 IN625, HT1 IN625/TiC, and HT2 IN625 conditions due to low concentration.

In order to investigate the evolution of the γ lattice parameter for the alloy and the composite, the Nelson-Riley method was used. The γ lattice parameter trend is reported in **Fig. 11** (c). The modification of the γ lattice parameter can be correlated with the microstructure evolution of the alloy and composite. More in detail, the dissolution of chemical elements inside the γ matrix tends to enlarge its lattice parameters, whereas the depletion of chemical elements to form phases reduces its lattice parameters [47,53,54].

The composite showed a slightly enlarged γ lattice parameter in the AB condition compared to the IN625 alloy. This result confirms that the high temperature involved in the melt pools leads to partial melt of the TiC particles, while the unmelted TiC particles tend to be pushed along the grain boundaries and melt pool contours, as discussed in paragraph 3.1. After the dissolution of TiC, the Ti enlarges the γ lattice parameter while the C tends to be enriched in the interdendritic areas, thus promoting the formation of new TiC or other MC carbides by the eutectic reaction.

After HT1, IN625 showed an increment of the γ lattice parameter compared to the AB condition due to an initial dissolution of the dendritic structures inside the γ matrix, while the composite exhibited a lattice parameter comparable with the AB condition, thanks to the stabilization effect of the TiC. After HT2, IN625 underwent full dendritic dissolution and chemical homogenization, which caused an increase in the γ lattice parameter [47]. Differently, the inhibited fully dendritic dissolution and recrystallization that occurred in IN625/TiC did not significantly affect the γ lattice parameter recorded in the AB condition. More in detail, the partial dendritic dissolution enlarged the γ lattice parameter by enriching chemical elements like Nb, Mo, and Ti from the interdendritic areas. On the contrary, the formation of Nb, Ti-rich MC carbides depleted part of these chemical elements inside the γ matrix, thus providing a contraction of the lattice parameter. The combination of the two mentioned phenomena produced limited γ lattice parameters.

This behavior can be associated with the high thermal stability induced by adding TiC to the IN625 alloy.

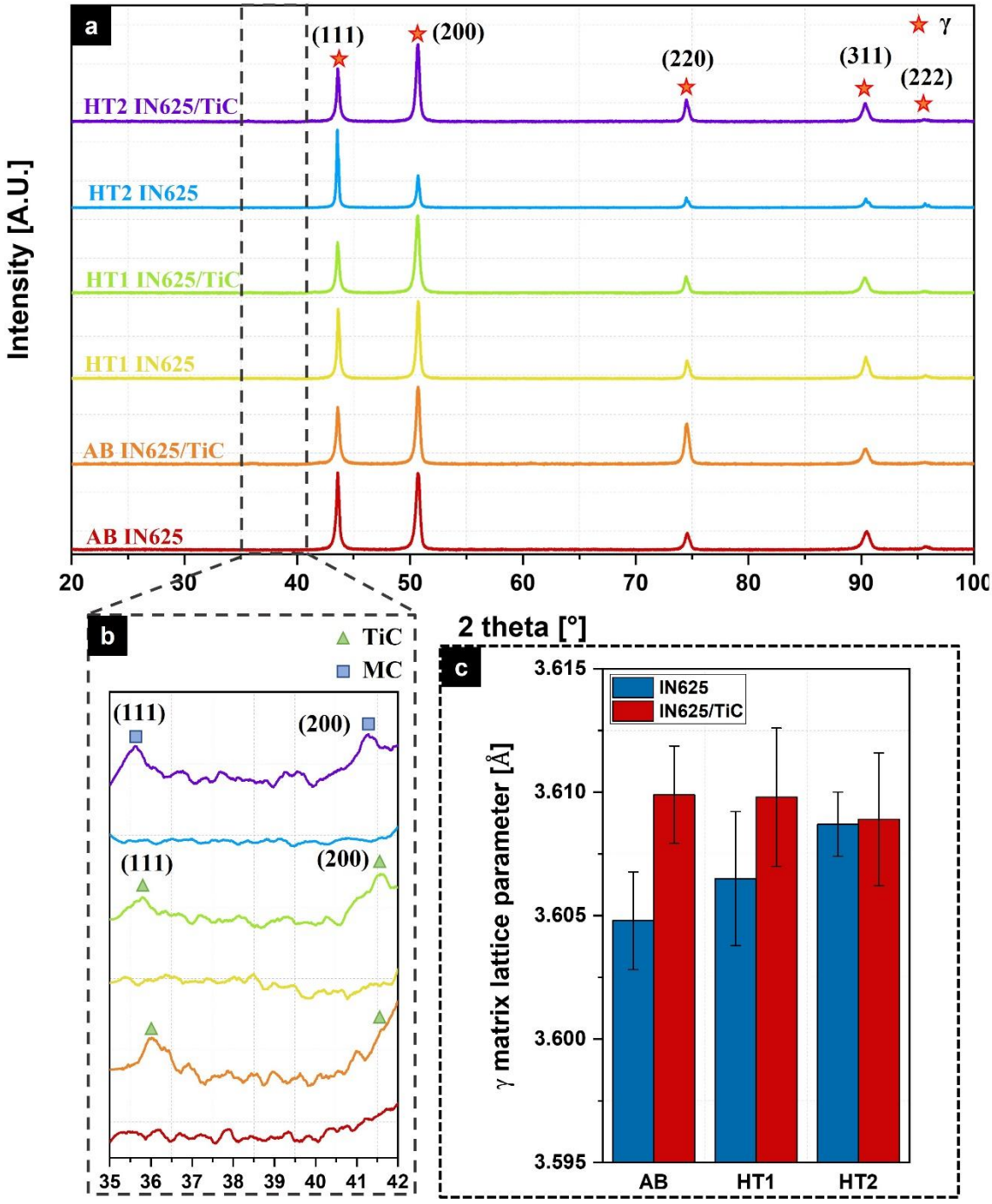

Fig. 11. (a) XRD spectrum IN625 and IN625/TiC; (b) zoom between 35 and 42° showing the peaks of the TiC and Nb,Ti-rich MC carbides for the AB, HT1 and HT2 IN625/TiC conditions; (c) γ lattice parameter evolution of IN625 and IN625/TiC under different heat treatments.

3.5 Mechanical properties and tensile fracture surfaces

The mechanical properties of the IN625 and IN625/TiC samples in the AB and heat-treated conditions are reported in **Fig. 12** (a and b) and **Table 3**.

Comparing IN625/TiC with IN625 in the AB condition, the mechanical properties presented an increment in hardness (+60 %), yield strength (+23 %), and ultimate tensile strength (+25 %) faced with a comparable value of elongation at failure. The increment of tensile strength and hardness could be attributed to the TiC particles triggering strengthening mechanisms, while the similar elongation at failure of the alloy and composite underlined that the low concentration of micro-segregations of TiC did not drastically modify the ductility.

Cheng et al. [22] found that the AB IN625 with 4wt % of nanoTiC presented an increment of the ultimate tensile strength of around 46 % and a decrement of ductility of around 31 % with respect to the IN625 alloy. In the current AB IN625/TiC, the lower mechanical property variations are consistent with adding a lower concentration of TiC particles inside the alloy.

In the AB state, the addition of 1wt% of sub-micrometric TiC increased the hardness from 238 HBW to 377 HBW. This latter value is superior to the hardness of the micrometric IN625/TiC 1wt% (312 HBW) processed in a previous work of our research group [31]. These results agree with the scenario described by Gu et al.[27] on developing IN625/TiC composite by DED, reporting the greater hardness improvement of finer TiC particles (like nanometric size) compared to the sub-micrometric TiC particles.

After annealing treatment, HT1 IN625/TiC showed higher hardness (+60 %), yield strength (+5 %), ultimate tensile strength (+9 %), and lower elongation at failure (-40 %) compared with HT1 IN625 alloy. For the composite, the superior mechanical properties combined with reduced ductility can be justified by the limited dendritic dissolution and the formation of MC carbides. On the other hand, in the IN625 alloy case, the more intense MC formation increased the tensile strength reducing the gap with the composite, whereas the dissolution of the dendritic structures improved its ductility.

Finally, after the solution annealing treatment, the HT2 IN625/TiC composite revealed the greatest variations in hardness (+100 %), yield strength (+86 %), ultimate tensile strength (+50 %), and elongation at failure (-45 %) compared to the HT2 IN625 alloy. In particular, for the composite, the limited dissolution of dendritic

structures and the grain size stabilization kept high hardness and tensile strength under solution annealing treatment. Furthermore, the formed small-size MC carbides inside grains induced an additional strengthening mechanism. On the contrary, IN625 underwent full dendritic dissolution and recrystallization, thus improving its ductility but drastically reducing hardness and tensile strength. In a previous work, the IN625/TiC with 1wt% of micrometric TiC under the same solution-annealed treatment (HT2 condition) revealed columnar grains and hardness values around 254 HBW [31]. However, the HT2 IN625/TiC with sub-micrometric TiC particles allowed the fabrication of a composite with an enhanced hardness of around 325 HBW, thus indicating a better reinforcement inside the alloy even after heat treatments.

In order to investigate the plastic behaviors of the composite and IN625 alloy, the strain hardening exponent (n) was determined by means of the Ludwik model using the true stress-strain data set of the specimens [40]. The analysis of the microstructures correlated with the calculated n values (**Fig. 12** (c and d),**Table 3**), brings to the following conclusions.

The worst strain hardening ability was observable in the AB condition for both the alloy and composite. This result can be explained by considering the dendritic structures characterized by the high amount of residual stresses and dislocation density, indicated by the high concentration of LAGBs and columnar deformed grains. Moreover, the load was applied perpendicular to the building direction, thus increasing the number of grain boundaries acting against the dislocation movement and reducing the strain hardening coefficient [42]. Since the TiC particles did not activate sensible grain refinement, as discussed in paragraph 3.2, the two n values were similar.

The strain hardening ability increased considerably in both materials after applying the heat treatments HT1 and HT2. After HT1, the major outcome is initial dendritic dissolution and stress relaxation, coupled with sub-micrometric and micrometric MC carbide precipitation along the grain boundaries (**Fig. 8** (a and b)). The dendritic dissolution provides less obstacle to the dislocation movement, while the intergranular carbides involve a limited action against the dislocation motion, thus enhancing alloy and composite hardening ability.

Conversely, the strain hardening ability after HT2 tends to be slightly lower than the HT1 condition for both IN625 and IN625/TiC conditions. This could be explained by considering the precipitation of small-size carbides inside the grains detected by TOF-SIMS analysis (**Fig. 10** Nb and Ti maps), which fully act as an obstacle to the dislocation motion. HT2 IN625/TiC presented slightly lower strain hardening ability (lower n) due to the partial stabilization of the dendritic structures induced by the TiC particles, while the HT2 IN625 alloy subjected to full dendritic dissolution presented higher strain hardening ability since the dislocation movements are less hindered, as also denoted by the low fraction of LAGBs.

Fig. 12 (c and d) shows the experimental curves and the corresponding interpolating lines. The two systems' behavior was similar, indicating that the amount of TiC had a minor impact on the alloy ductility. Nonetheless, the IN625 alloy had a considerably broader set of possible true stress values, which could be related to the microstructure evolution under heat treatment. At the same time, the composite showed three sets of data extremely close, one to each other, a further confirmation that this composite had strong microstructural stability.

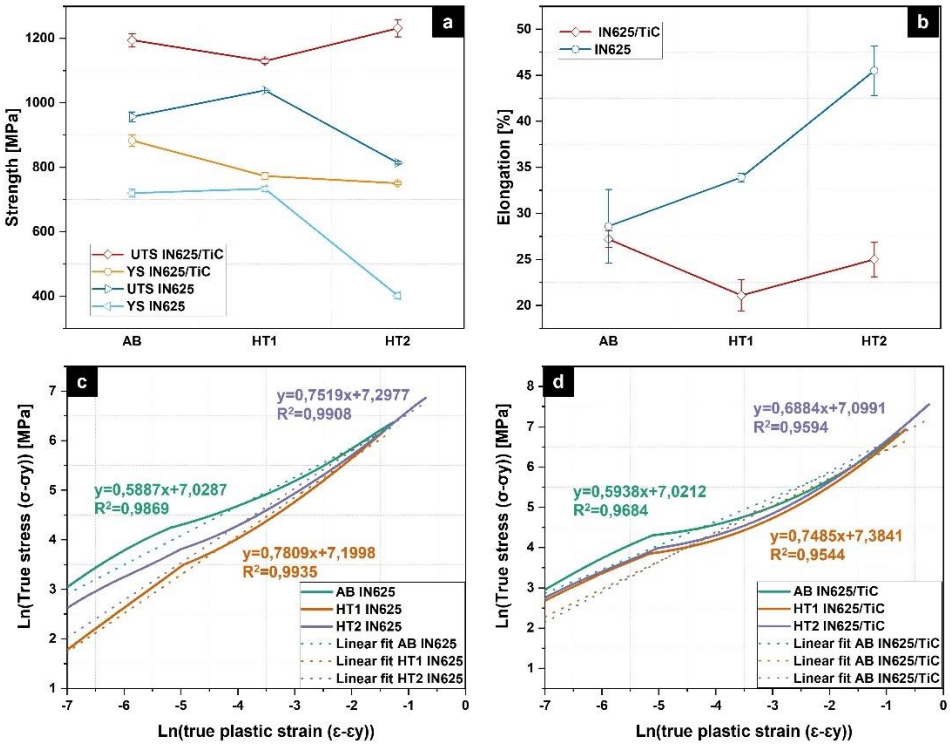

Fig. 12 (a) yield strength (YS) and ultimate tensile strength (UTS), (b) elongation at failure (ε_f) results of tensile specimens of IN625 and IN625/TiC in the AB, HT1, and HT2 conditions. Ludwik fitting plot for (c) IN625 and (d) IN625/TiC in AB HT1 and HT2 condition

Table 3 Brinell Hardness, yield strength (YS), ultimate tensile strength (UTS), elongation at failure (ε_f) and strain hardening coefficient (n) results of IN625 and IN625/TiC specimens in AB, HT1, and HT2 conditions compared with the literature [22] [31]. nano (abbreviation for nanometric); and micro (abbreviation for micrometric). Strain hardening exponent (abbreviated as n).

Condition	Hardness [HBW]	YS [MPa]	UTS [MPa]	ε_f [%]	n
AB IN625	238 ± 4	723 ± 24	957 ± 15	29 ± 4	0.588
AB IN625/TiC	377 ± 3	883 ± 17	1195 ± 20	27 ± 1	0.594
AB IN625 [22]	/	/	836	~45	/
AB IN625/nano-TiC 4 wt% [22]	/	/	1219	~31	/
AB IN625/micro-TiC 1 wt% [31]	312 ± 5	/	/	/	/
HT1 IN625	220 ± 1	733 ± 8	1039 ± 1	34 ± 1	0.780
HT1 IN625/TiC	347 ± 2	773 ± 11	1130 ± 7	21 ± 2	0.748
HT2 IN625	161 ± 4	394 ± 7	814 ± 4	45 ± 3	0.750
HT2 IN625/TiC	325 ± 4	750 ± 4	1231 ± 27	25 ± 2	0.688
HT2 IN625/micro-TiC 1wt% [31]	256 ± 4	/	/	/	/

All the fracture surfaces can be classified as mixed ductile and brittle fractures **Fig. 13** (a-f) [55–57]. In particular, in **Fig. 13** (a-f), yellow arrows pointed out micro-voids (typical of ductile fractures), while the red arrows highlighted smooth facets (typical of brittle fractures).

The AB IN625 (**Fig. 13** (a)) and AB IN625/TiC (**Fig. 13** (b)) show similar fracture surfaces with micro-void coalescence and fine dimples coupled to brittle fracture zones. In the case of the IN625 alloy, the brittle fractures can derive from segregations in the interdendritic areas or precipitates like NbC carbides [49]. In addition, for the composite, the TiC particles and the micro-segregations of TiC could provide further points for triggering cleavage-like features. Comparing the HT1 IN625 (**Fig. 13** (c)) and HT1 IN625/TiC (**Fig. 13** (d)) conditions, the composite revealed more smooth zones, thus justifying the lower elongation at failure compared to the alloy. In fact, the composite presented dendritic structures and the formed carbides, providing additional weaker points for brittle fractures. On the other hand, for the HT1 IN625 condition, the dendritic dissolution limited the possible zones subjected to brittle fractures, thus improving its ductility.

The comparison of the fracture surface of HT2 IN625 (**Fig. 13** (e)) and HT2 IN625/TiC (**Fig. 13** (f)) denoted a substantial variation between the two conditions. The composite presented a high frequency of cleavage-like features triggered by the presence of carbides as well as the network of dendritic architectures. Differently, the HT2 IN625 condition was mainly dominated by ductile fractures with large micro-voids and fine dimples due to the full dissolution of dendritic structures and recrystallization.

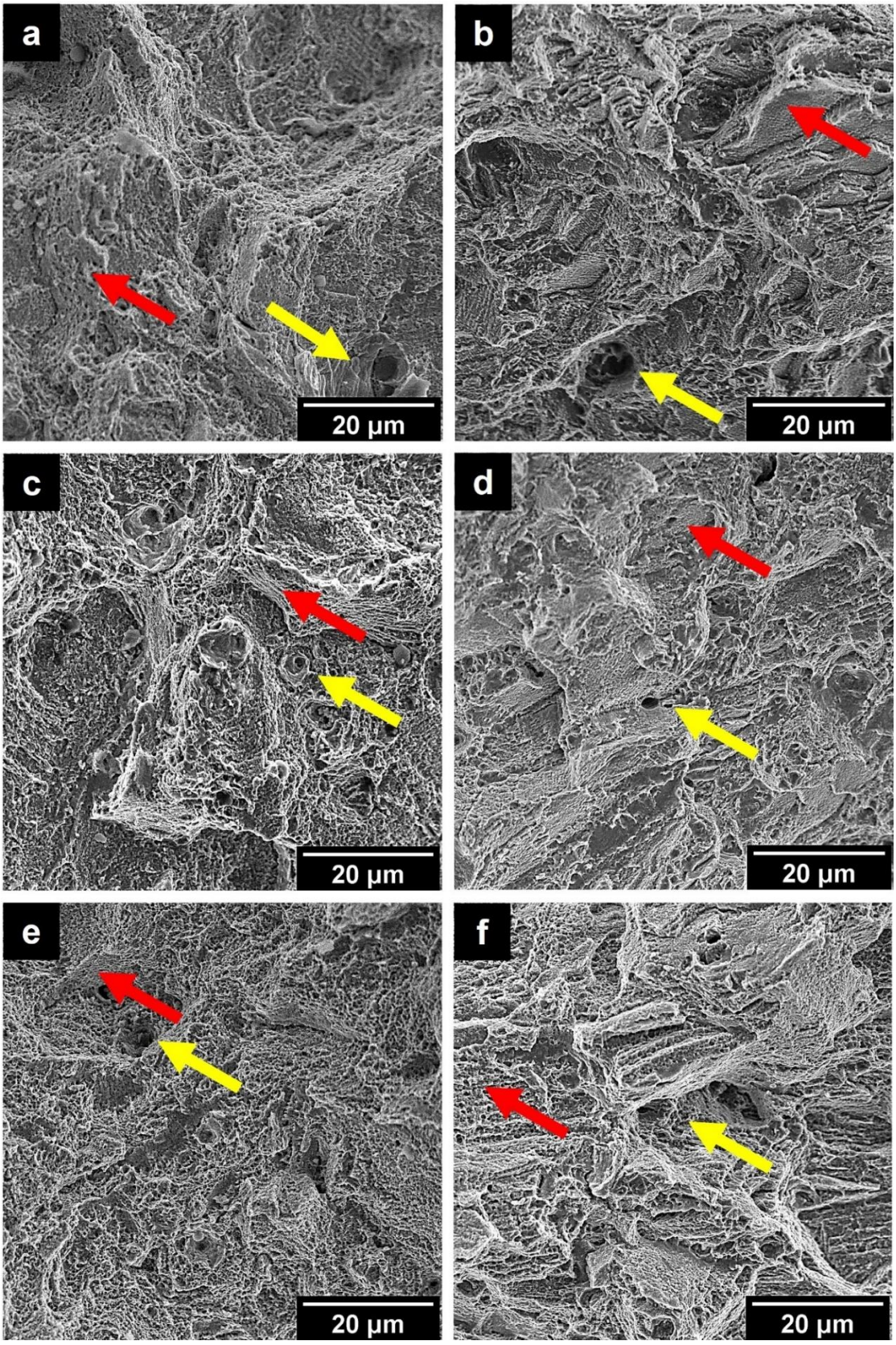

Fig. 13. (a-f) SEM images of tensile fracture surface morphologies respectively for IN625 and IN625/TiC in AB (a and b), HT1 (c and d), and HT2 (e and f) states. Yellow and red arrows underline micro-voids and smooth facets, respectively.

4. Conclusions

In this study, Inconel 625 alloy and Inconel 625 reinforced with 1wt% of sub-micrometric TiC particles were successfully produced by LPBF. The microstructure and mechanical properties evolution of the as-built and heat-treated conditions were investigated. The primary results can be summarized as follows:

1. The composite powder with sub-micrometric TiC presented a higher flow rate than composite powder with micrometric TiC, thus reducing the possibility of creating an inhomogeneous powder spreading during the LPBF process, which may provoke defects inside the component.
2. A set of process parameters involving a VED of 99 J/mm^3 allowed the fabrication of dense IN625 and IN625/TiC production. Using this VED, porosity levels below 0.15% were guaranteed, and good dispersion of TiC particles was reached in the composite. However, a few micro-segregations of TiC were still detectable in the IN625/TiC composite.
3. The AB IN625 and AB IN625/TiC conditions revealed columnar grains with a similar content of recrystallized grains, concentration of LAGBs and sub-micrometric dendritic structures for the AB IN625 and AB IN625/TiC. A very limited grain refinement was detected due to the low quantity of added TiC particles in the alloy. The γ lattice parameter was slightly larger for the composite than the alloy, indicating a partial dissolution of TiC particles during the LPBF process. For the composite, the TiC particles tend to be located along the grain boundaries, melt pool contours, and interdendritic regions.
4. After annealing treatment (HT1), both IN625 and IN625/TiC specimens still presented columnar grains with a frequency of recrystallized grains and grain sizes equal to the AB conditions. The IN625 alloy showed a slight reduction of the LAGBs differently from the composite that presented a stabilization of the LAGBs. The increase in the γ lattice parameter of the IN625 alloy confirmed the initial dissolution of the dendritic structure, which is strongly limited in the composite. The microstructure analysis revealed the formation of new MC carbides mainly located along the grain boundaries in both alloy and composite.
5. Solution heat treatment (HT2) triggered recrystallization in IN625 with equiaxed and twin grains, leading to a recrystallized grains percentage of 96% and LAGBs frequency of around 5 %. Conversely, the HT2 IN625/TiC still showed columnar grains with fine dendritic structures, keeping the GOS trend and the level of LAGBs similar to the AB and HT1 condition around 50%. The IN625 showed the largest γ lattice parameter due to the chemical homogenization, while the composite presented a γ lattice parameter similar

to the AB condition thanks to the stabilization effect of the TiC particles, reducing the dendritic dissolution. Moreover, the high temperature involved the formation of Nb,Ti-rich MC carbides in both the alloy and composite. The composite presented micrometric carbides, while the alloy showed sub-micrometric carbides.

6. The addition of 1wt% of sub-micrometric TiC into the IN625 alloy increased the hardness (around 60 %) and ultimate tensile strength (around 25 %) in AB condition, keeping the ductility value similar to IN625 alloy. After HT1, the limited dissolution of the dendritic structure and the formation of MC carbides preserved high hardness and tensile strength but simultaneously reduced its ductility compared to the HT1 IN625. Finally, TiC particles hinder the recrystallization and grain growth under HT2, providing limited hardness and tensile strength variations for the composite. In detail, the HT2 IN625/TiC presented an increased hardness (around 100 %) and ultimate tensile strength (around 50 %) compared to the HT2 IN625 alloy. However, the HT2 IN625/TiC showed a lower ductility (around 45 %) with respect to the HT2 IN625 alloy. The correlation between strain hardening exponent (n) and microstructure underlined the differences in the AB and HT conditions. The AB conditions revealed the lowest strain hardening ability due to the high concentration of dislocation density and fine dendritic structures hindering the dislocation movements. After HT1, the strain hardening ability was improved by the relaxation of the residual stresses and the initial dissolution of dendritic structures. Finally, HT2 revealed an intermedia strain hardening ability derived from the small MC carbides, which restricted the movement of the dislocations.

7. The base alloy and composite in AB condition showed a balanced ratio between microvoids coalescence areas and brittle facets. However, the heat-treated IN625/TiC presented a more elevated frequency of smooth fractures due to the formation of new carbides and the limited dissolution of the network of dendritic architectures. Conversely, the heat-treated IN625 underwent dendritic dissolution (for HT1) and a strong chemical homogenization and recrystallization (for HT2), which increased its ductility, thus exhibiting mainly large micro-voids and fine dimples.

The current study shows that the IN625/TiC composite with only 1wt% of submicrometric TiC particles could significantly increment the tensile properties and improve its thermal stability, using the same process window parameter of the IN625 alloy.

Data Availability: The data presented in this study are available on request from the corresponding author.

Declaration of competing interest: The authors declare that they have no known competing financial interests or personal relationships that could have appeared to influence the work reported in this paper.

Acknowledgments: The authors would like to thank Ms. Marta Corino for supporting a part of the metallographic preparation during this research activity.

Appendix A

The inverse pole figure (IPF) YO maps of the IN625 and IN625/TiC and the pole figure are reported in the **Fig. 1 A**, **Fig. 2 A** respectively.

From the EBSD analyses, there is a preferential texture along the {100} direction for all the IN625 and IN625/TiC conditions, although other orientations are visible, except for the HT2 IN625 state characterized by recrystallization phenomenon. The preferential growth of columnar grains along the {100} is commonly reported for the fcc γ phase when processed by laser additive manufacturing processes [58,59]. A strong cubic fiber {100} direction could be developed using more energetic parameters. Finally, it is interesting to note that the pole figure of the composites presented a greater maximum texture intensity due to the addition of TiC particles that generate high laser absorptivity, and, consequently, more elevated melt pool temperatures, enhancing the overall intensity of the texture.

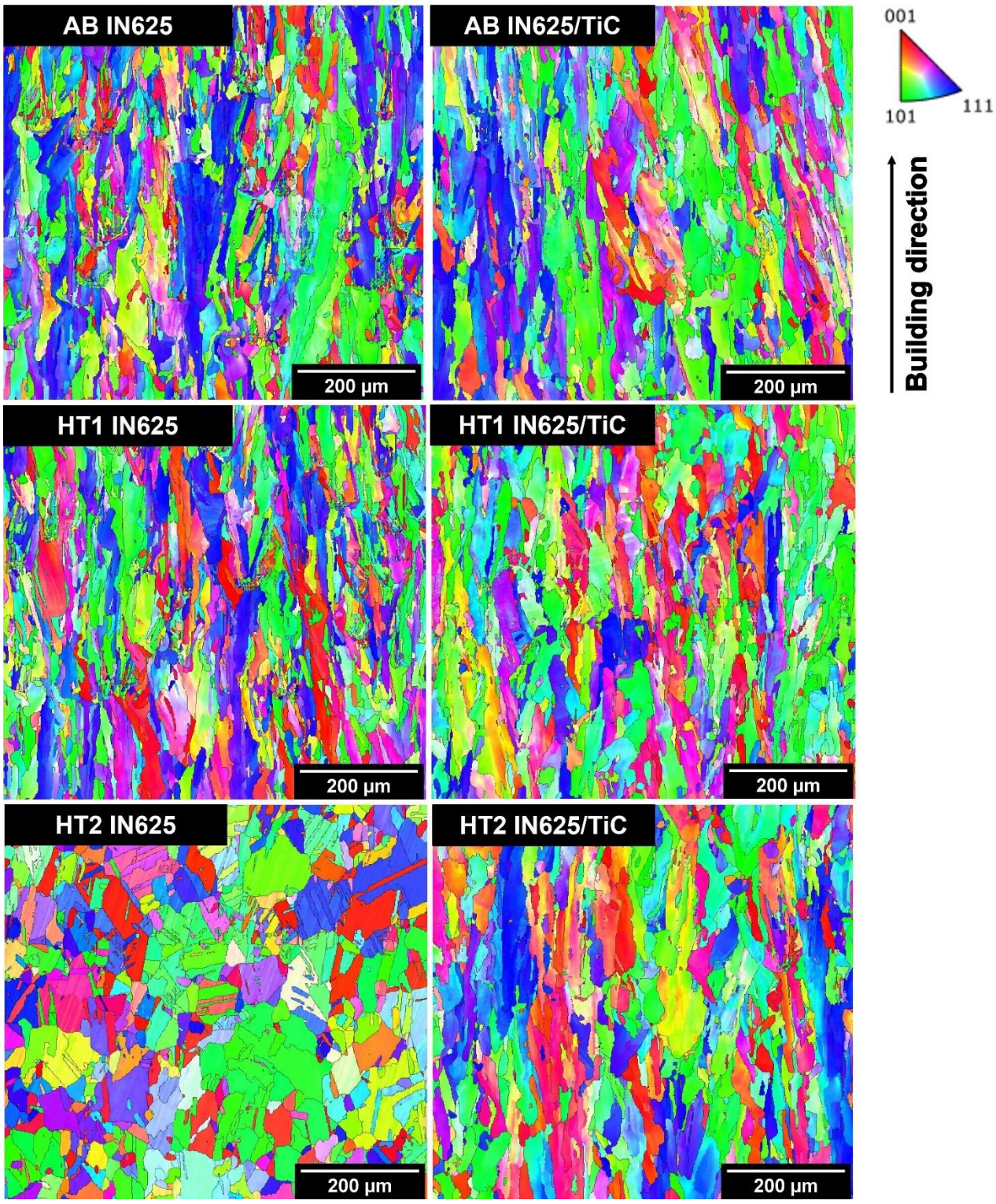

Fig. 1A EBSD inverse pole figure YO maps of the IN625 and IN625/TiC in the AB and HT conditions along the building direction.

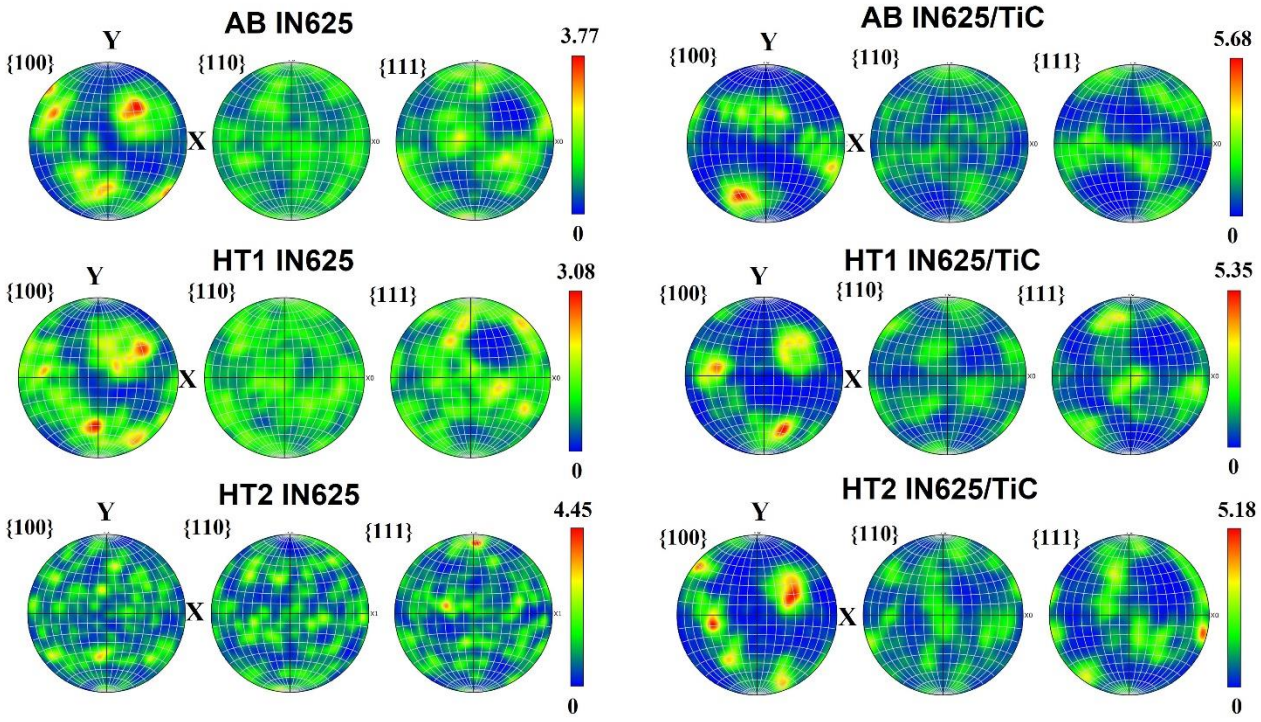

Fig. 2A Pole Figure of the IN625 and IN625/TiC in the AB and HT conditions

References

[1] M.M. Attallah, R. Jennings, X. Wang, L.N. Carter, Additive manufacturing of Ni-based superalloys: The outstanding issues, MRS Bull. 41 (2016) 758–764. https://doi.org/10.1557/mrs.2016.211.

[2] K.C. Tekin, U. Malayoglu, Assessing the tribocorrosion performance of three different nickel-based superalloys, Tribol Lett. 37 (2010) 563–572. https://doi.org/10.1007/s11249-009-9552-1.

[3] K. Mahesh, J.T. Philip, S.N. Joshi, B. Kuriachen, Machinability of Inconel 718: A critical review on the impact of cutting temperatures, Materials and Manufacturing Processes. 36 (2021) 753–791. https://doi.org/10.1080/10426914.2020.1843671.

[4] Y.C. Lin, H. Yang, L. Li, Effects of solutionizing cooling processing on γ″ (Ni3Nb) phase and work hardening characteristics of a Ni-Fe-Cr-base superalloy, Vacuum. 144 (2017) 86–93. https://doi.org/10.1016/j.vacuum.2017.07.025.

[5] Reed R. C., Superalloys - Fundamentals and Applications, in: Cambridge , 2006: pp. 33–120.

[6] S. Floreen, G.E. Fuchs, W.J. Yang, The Metallurgy of Alloy 625, in: Superallys 718,625,706 and Various Derivatives, 1994: pp. 13–37.

[7] Donachie M.J., Donachie S.J., SUPERALLOYS Second Edition, OH, USA, 2002.

[8] W. Akhtar, J. Sun, P. Sun, W. Chen, Z. Saleem, Tool wear mechanisms in the machining of Nickel based super-alloys: A review, Frontiers of Mechanical Engineering. 9 (2014) 106–119. https://doi.org/10.1007/s11465-014-0301-2.

[9] Z. Liu, D. Zhao, P. Wang, M. Yan, C. Yang, Z. Chen, J. Lu, Z. Lu, Additive manufacturing of metals: Microstructure evolution and multistage control, J Mater Sci Technol. 100 (2022) 224–236. https://doi.org/10.1016/j.jmst.2021.06.011.

[10] B. Graybill, M. Li, D. Malawey, C. Ma, J.-M. Alvarado-Orozco, E. Martinez-Franco, Additive, in: Proceedings of the ASME 2018 13th International Manufacturing Science and Engineering Conference, 2018.

[11] M. Karmuhilan, S. Kumanan, A Review on Additive Manufacturing Processes of Inconel 625, J Mater Eng Perform. 31 (2022) 2583–2592. https://doi.org/10.1007/s11665-021-06427-3.

[12] S. Li, Q. Wei, Y. Shi, C.K. Chua, Z. Zhu, D. Zhang, Microstructure Characteristics of Inconel 625 Superalloy Manufactured by Selective Laser Melting, J Mater Sci Technol. 31 (2015) 946–952. https://doi.org/10.1016/j.jmst.2014.09.020.

[13] L.N. Carter, X. Wang, N. Read, R. Khan, M. Aristizabal, K. Essa, M.M. Attallah, Process optimisation of selective laser melting using energy density model for nickel based superalloys, Materials Science and Technology (United Kingdom). 32 (2016) 657–661. https://doi.org/10.1179/1743284715Y.0000000108.

[14] A. Kreitcberg, V. Brailovski, S. Turenne, Elevated temperature mechanical behavior of IN625 alloy processed by laser powder-bed fusion, Materials Science and Engineering A. 700 (2017) 540–553. https://doi.org/10.1016/j.msea.2017.06.045.

[15] V. Shankar, K. Bhanu, S. Rao, S.L. Mannan, Microstructure and mechanical properties of Inconel 625 superalloy, Journal of Nuclear Materials . 288 (2001) 222–232. https://doi.org/https://doi.org/10.1016/S0022-3115(00)00723-6.

[16] L.M. Suave, J. Cormier, P. Villechaise, A. Soula, Z. Hervier, D. Bertheau, J. Laigo, Microstructural evolutions during thermal aging of alloy 625: Impact of temperature and forming process, Metall Mater Trans A Phys Metall Mater Sci. 45 (2014) 2963–2982. https://doi.org/10.1007/s11661-014-2256-7.

[17] Z. Wang, S. Gao, S. Li, W. Zhang, L. Lan, Y. Jiang, B. He, Research Progress of Laser Additive Manufacturing Nickel-Based Alloy Metal Matrix Composites, Metals (Basel). 13 (2023). https://doi.org/10.3390/met13010129.

[18] M. Ostolaza, J.I. Arrizubieta, A. Lamikiz, S. Plaza, N. Ortega, Latest Developments to Manufacture Metal Matrix Composites and Functionally Graded Materials through AM: A State-of-the-Art Review, Materials. 16 (2023). https://doi.org/10.3390/ma16041746.

[19] B. Zhang, G. Bi, P. Wang, J. Bai, Y. Chew, M.S. Nai, Microstructure and mechanical properties of Inconel 625/nano-TiB2 composite fabricated by LAAM, Mater Des. 111 (2016) 70–79. https://doi.org/10.1016/j.matdes.2016.08.078.

[20] M.Z. Ghodsi, S. Khademzadeh, E. Marzbanrad, M.H. Razmpoosh, N. De Marchi, E. Toyserkani, Development of Yttria-stabilized zirconia reinforced Inconel 625 metal matrix composite by laser powder bed fusion, Materials Science and Engineering A. 827 (2021). https://doi.org/10.1016/j.msea.2021.142037.

[21] D.E. Cooper, N. Blundell, S. Maggs, G.J. Gibbons, Additive layer manufacture of Inconel 625 metal matrix composites, reinforcement material evaluation, J Mater Process Technol. 213 (2013) 2191–2200. https://doi.org/10.1016/j.jmatprotec.2013.06.021.

[22] L. Chen, Y. Sun, L. Li, X. Ren, Microstructure evolution, mechanical properties, and strengthening mechanism of TiC reinforced Inconel 625 nanocomposites fabricated by selective laser melting, Materials Science and Engineering A. 792 (2020). https://doi.org/10.1016/j.msea.2020.139655.

[23] T. Lee, W. Jeong, S.H. Chung, H.J. Ryu, Effects of TiC on the microstructure refinement and mechanical property enhancement of additive manufactured Inconel 625/TiC metal matrix composites fabricated with novel core-shell composite powder, J Mater Sci Technol. 164 (2023) 13–26. https://doi.org/10.1016/j.jmst.2023.04.033.

[24] F. Zafar, O. Emadinia, J. Conceição, M. Vieira, A. Reis, A Review on Direct Laser Deposition of Inconel 625 and Inconel 625-Based Composites—Challenges and Prospects, Metals (Basel). 13 (2023). https://doi.org/10.3390/met13040787.

[25] C. Hong, D. Gu, D. Dai, M. Alkhayat, W. Urban, P. Yuan, S. Cao, A. Gasser, A. Weisheit, I. Kelbassa, M. Zhong, R. Poprawe, Laser additive manufacturing of ultrafine TiC particle reinforced Inconel 625 based composite parts: Tailored microstructures and enhanced performance, Materials Science and Engineering A. 635 (2015) 118–128. https://doi.org/10.1016/j.msea.2015.03.043.

[26] G. Bi, C.N. Sun, M.L. Nai, J. Wei, Micro-structure and mechanical properties of nano-TiC reinforced Inconel 625 deposited using LAAM, Phys Procedia. 41 (2013) 828–834. https://doi.org/10.1016/j.phpro.2013.03.155.

[27] D. Gu, S. Cao, K. Lin, Laser Metal Deposition Additive Manufacturing of TiC Reinforced Inconel 625 Composites: Influence of the Additive TiC Particle and Its Starting Size, Journal of Manufacturing Science and Engineering, Transactions of the ASME. 139 (2017). https://doi.org/10.1115/1.4034934.

[28] S. Cao, D. Gu, Q. Shi, Relation of microstructure, microhardness and underlying thermodynamics in molten pools of laser melting deposition processed TiC/Inconel 625 composites, J Alloys Compd. 692 (2017) 758–769. https://doi.org/10.1016/j.jallcom.2016.09.098.

[29] L. Chen, Y. Sun, L. Li, Y. Ren, X. Ren, In situ TiC/Inconel 625 nanocomposites fabricated by selective laser melting: Densification behavior, microstructure evolution, and wear properties, Appl Surf Sci. 518 (2020). https://doi.org/10.1016/j.apsusc.2020.145981.

[30] L. Chen, Y. Sun, L. Li, X. Ren, Effect of heat treatment on the microstructure and high temperature oxidation behavior of TiC/Inconel 625 nanocomposites fabricated by selective laser melting, Corros Sci. 169 (2020). https://doi.org/10.1016/j.corsci.2020.108606.

[31] G. Marchese, A. Aversa, E. Bassini, Microstructure and hardness evolution of solution annealed inconel 625/tic composite processed by laser powder bed fusion, Metals (Basel). 11 (2021). https://doi.org/10.3390/met11060929.

[32] H. Chandler, Heat Treater's Guide: Practices and Procedures for Nonferrous Alloys, ASM International, OH, USA, 1996, n.d.

[33] Y. Cao, H. Di, J. Zhang, J. Zhang, T. Ma, R.D.K. Misra, An electron backscattered diffraction study on the dynamic recrystallization behavior of a nickel-chromium alloy (800H) during hot deformation, Materials Science and Engineering A. 585 (2013) 71–85. https://doi.org/10.1016/j.msea.2013.07.037.

[34] T.S. Prithiv, P. Bhuyan, S.K. Pradhan, V. Subramanya Sarma, S. Mandal, A critical evaluation on efficacy of recrystallization vs. strain induced boundary migration in achieving grain boundary engineered microstructure in a Ni-base superalloy, Acta Mater. 146 (2018) 187–201. https://doi.org/10.1016/j.actamat.2017.12.045.

[35] A. Hadadzadeh, F. Mokdad, M.A. Wells, D.L. Chen, A new grain orientation spread approach to analyze the dynamic recrystallization behavior of a cast-homogenized Mg-Zn-Zr alloy using electron backscattered diffraction, Materials Science and Engineering A. 709 (2018) 285–289. https://doi.org/10.1016/j.msea.2017.10.062.

[36] R.A. Al-Hammadi, R. Zhang, C. Cui, Z. Zhou, Y. Zhou, Effect of strain rate on microstructure evolution of a fine-grained γ + γ' Ni-Co-base superalloy during superplasticity, Mater Charact. 203 (2023) 113112. https://doi.org/10.1016/j.matchar.2023.113112.

[37] C. Li, Y. Tian, Y. Chen, P. Hodgson, X. Wu, Y. Zhu, A. Huang, Hierarchical layered and refined grain structure of Inconel 718 superalloy produced by rolling-assisted directed energy deposition, Additive Manufacturing Letters. 1 (2021) 100009. https://doi.org/10.1016/j.addlet.2021.100009.

[38] Q. Yang, L.R. Zhao, Characterization of nano-layered multilayer coatings using modified Bragg law, Mater Charact. 59 (2008) 1285–1291. https://doi.org/10.1016/j.matchar.2007.11.001.

[39] J.B. Nelson, D.P. Riley, An experimental investigation of extrapolationmethods in the derivation of accurate unit-celldimensions of crystals, Proceedings of the Physical Society. 57 (1945) 160–177.

[40] M. Liu, Q. Wang, Y. Cai, D. Lu, T. Wang, Y. Pei, H. Zhang, Y. Liu, Q. Wang, Comparison in deformation behavior, microstructure, and failure mechanism of nickel base alloy 625 under two strain rates, Materials. 14 (2021). https://doi.org/10.3390/ma14102652.

[41] N. Afrin, D.L. Chen, X. Cao, M. Jahazi, Strain hardening behavior of a friction stir welded magnesium alloy, Scr Mater. 57 (2007) 1004–1007. https://doi.org/10.1016/j.scriptamat.2007.08.001.

[42] L. Ladani, Additive Manufacturing of Metals Materials, Processes, Tests, and Standards, 2021.

[43] M. Sadowski, L. Ladani, W. Brindley, J. Romano, Optimizing quality of additively manufactured Inconel 718 using powder bed laser melting process, Addit Manuf. 11 (2016) 60–70. https://doi.org/10.1016/j.addma.2016.03.006.

[44] J.P. Kruth, G. Levy, F. Klocke, T.H.C. Childs, Consolidation phenomena in laser and powder-bed based layered manufacturing, CIRP Ann Manuf Technol. 56 (2007) 730–759. https://doi.org/10.1016/j.cirp.2007.10.004.

[45] L. Ladani, J. Romano, W. Brindley, S. Burlatsky, Effective liquid conductivity for improved simulation of thermal transport in laser beam melting powder bed technology, Addit Manuf. 14 (2017) 13–23. https://doi.org/10.1016/j.addma.2016.12.004.

[46] C. Li, R. White, X.Y. Fang, M. Weaver, Y.B. Guo, Microstructure evolution characteristics of Inconel 625 alloy from selective laser melting to heat treatment, Materials Science and Engineering: A. 705 (2017) 20–31. https://doi.org/10.1016/j.msea.2017.08.058.

[47] G. Marchese, S. Parizia, M. Rashidi, A. Saboori, D. Manfredi, D. Ugues, M. Lombardi, E. Hryha, S. Biamino, The role of texturing and microstructure evolution on the tensile behavior of heat-treated Inconel 625 produced via laser powder bed fusion, Materials Science and Engineering A. 769 (2020). https://doi.org/10.1016/j.msea.2019.138500.

[48] P.V. Cobbinah, R.A. Nzeukou, O.T. Onawale, W.R. Matizamhuka, Laser powder bed fusion of potential superalloys: A review, Metals (Basel). 11 (2021) 1–37. https://doi.org/10.3390/met11010058.

[49] G. Marchese, M. Lorusso, S. Parizia, E. Bassini, J.W. Lee, F. Calignano, D. Manfredi, M. Terner, H.U. Hong, D. Ugues, M. Lombardi, S. Biamino, Influence of heat treatments on microstructure evolution and mechanical properties of Inconel 625 processed by laser powder bed fusion, Materials Science and Engineering A. 729 (2018) 64–75. https://doi.org/10.1016/j.msea.2018.05.044.

[50] T. Keller, G. Lindwall, S. Ghosh, L. Ma, B.M. Lane, F. Zhang, U.R. Kattner, E.A. Lass, J.C. Heigel, Y. Idell, M.E. Williams, A.J. Allen, J.E. Guyer, L.E. Levine, Application of finite element, phase-field, and CALPHAD-based methods to additive manufacturing of Ni-based superalloys, Acta Mater. 139 (2017) 244–253. https://doi.org/10.1016/j.actamat.2017.05.003.

[51] L.E. Shoemaker, ALLOYS 625 AND 725: TRENDS IN PROPERTIES AND APPLICATIONS, in: Superalloys 718, 625, 706 and Derivatives , 2005: pp. 409–418.

[52] J. Nie, Y. Wu, P. Li, H. Li, X. Liu, Morphological evolution of TiC from octahedron to cube induced by elemental nickel, CrystEngComm. 14 (2012) 2213–2221. https://doi.org/10.1039/c1ce06205k.

[53] A. Kreitcberg, V. Brailovski, S. Turenne, Elevated temperature mechanical behavior of IN625 alloy processed by laser powder-bed fusion, Materials Science and Engineering: A. 700 (2017) 540–553. https://doi.org/10.1016/j.msea.2017.06.045.

[54] S.K. Rai, A. Kumar, V. Shankar, T. Jayakumar, K.B.S. Rao, B. Raj, Characterization of microstructures in Inconel 625 using X-ray diffraction peak broadening and lattice parameter measurements, Scr Mater. 51 (2004) 59–63. https://doi.org/10.1016/j.scriptamat.2004.03.017.

[55] J. Luis González-Velázquez, Fractography and Failure Analysis, Springer, Charm, 2018.

[56] C.U. Brown, G. Jacob, M. Stoudt, S. Moylan, J. Slotwinski, A. Donmez, Interlaboratory Study for Nickel Alloy 625 Made by Laser Powder Bed Fusion to Quantify Mechanical Property Variability, J Mater Eng Perform. 25 (2016) 3390–3397. https://doi.org/10.1007/s11665-016-2169-2.

[57] A. Kreitcberg, V. Brailovski, S. Turenne, Effect of heat treatment and hot isostatic pressing on the microstructure and mechanical properties of Inconel 625 alloy processed by laser powder bed fusion, Materials Science and Engineering A. 689 (2017) 1–10. https://doi.org/10.1016/j.msea.2017.02.038.

[58] L.L. Parimi, G. Ravi, D. Clark, M.M. Attallah, Microstructural and texture development in direct laser fabricated IN718, Mater Charact. 89 (2014) 102–111. https://doi.org/10.1016/j.matchar.2013.12.012.

[59] A. Keshavarzkermani, M. Sadowski, L. Ladani, Direct metal laser melting of Inconel 718: Process impact on grain formation and orientation, J Alloys Compd. 736 (2018) 297–305. https://doi.org/10.1016/j.jallcom.2017.11.130.